POLITECNICO DI TORINO
Repository ISTITUZIONALE

Enhanced electrocatalytic oxygen reduction to HO with high selectivity via 2D 1T-MoS integrated with functionalized carbon nanohorns

*Original*
Enhanced electrocatalytic oxygen reduction to HO with high selectivity via 2D 1T-MoS integrated with functionalized carbon nanohorns / Wang, M., Benazzato, S., Cieszyski, ., Crisci, M., Pozzati, M., Calvillo, L., Wang, Y., Zhou, Y., Menna, E., Osella, S., Zeng, J., Gatti, T.. - In: NPJ 2D MATERIALS AND APPLICATIONS. - ISSN 2397-7132. - (2026). [10.1038/s41699-026-00752-8]

*Availability:*
This version is available at: 11583/3018149 since: 2026-11-19T09:12:17Z

*Publisher:*
Springer Nature

*Published*
DOI:10.1038/s41699-026-00752-8

*Terms of use:*

This article is made available under terms and conditions as specified in the corresponding bibliographic description in the repository

*Publisher copyright*

(Article begins on next page)

29 November 2026

npj | 2D materials and applications

Article

Published in partnership with FCT NOVA with the support of E-MRS

Article in Press

https://doi.org/10.1038/s41699-026-00752-8

# Enhanced electrocatalytic oxygen reduction to $H_2O$ with high selectivity via 2D 1T-$MoS_2$ integrated with functionalized carbon nanohorns

Check for updates

Mengjiao Wang[1] ✉, Stefania Benazzato[2], Łukasz Cieszyński[3], Matteo Crisci[4], Micaela Pozzati[1], Laura Calvillo[2], Yongying Wang[1], Yazhou Zhou[5], Enzo Menna[2,6] ✉, Silvio Osella[3], Juqin Zeng[1,7] & Teresa Gatti[1,4] ✉

Developing cost-effective and high-performance electrocatalysts for the oxygen reduction reaction (ORR) is essential for advancing anion-exchange membrane fuel cell technologies. In this study, we report a robust heterostructure formed by covalently functionalized carbon nanohorns (CNH-N) integrated with metallic 1T-MoS2 2D nanosheets. Through tailored diazonium chemistry, positively charged ammonium groups were introduced onto CNHs, enabling strong electrostatic and van der Waals interactions with negatively charged exfoliated $MoS_2$. Structural and spectroscopic analyses confirm successful functionalization, enhanced defect modulation, and intimate CNH–$MoS_2$ coupling. The resulting CNH-N-$MoS_2$ catalyst exhibits remarkable ORR performance, including an optimized onset potential of 0.80 V, reduced charge-transfer resistance, and a dominant four-electron reduction pathway with ~94% selectivity toward $H_2O$, which is comparable to commercial Pt/C. These results highlight how controlled chemical functionalization and heterointerface engineering can synergistically enhance catalytic activity and stabilize the 1T-MoS2 phase. The CNH-N-$MoS_2$ heterostructures thus represent a promising class of platinum-group-metal-free/low-metal-content electrocatalysts for efficient fuel cell applications.

The development of anion-exchange membrane fuel cells (AEMFCs) is considered an important step toward a sustainable energy future owing to their safe operation, low environmental impact, and potential for energy-efficient electricity generation. However, the sluggish kinetics of the oxygen reduction reaction (ORR) at the cathode, together with the possibility of incomplete oxygen reduction, significantly limits the efficiency and performance of AEMFCs[1]. Consequently, the development of highly active and selective ORR electrocatalysts capable of promoting the complete four-electron reduction of $O_2$ to $H_2O$ at low overpotentials has become a major research focus. Platinum-based catalysts remain the benchmark ORR catalysts because of their exceptional activity and stability, yet their high cost severely restricts the large-scale commercialization of fuel-cell technologies[2]. As a result, considerable efforts have been devoted to developing low-cost platinum-group-metal-free electrocatalysts.

Among the various candidates investigated, two-dimensional (2D) transition metal dichalcogenides (TMDCs) have emerged as promising ORR electrocatalysts owing to their layered structures, high surface area, tunable electronic properties, and abundance of catalytically active sites[3,4]. In particular, $MoS_2$ has attracted significant attention because of its low cost, scalability, and widespread availability[5]. Mass-produced $MoS_2$ nanosheets have already been employed as screen-printed ORR electrodes, highlighting their practical potential[6]. The catalytic performance of $MoS_2$ originates from its edge sites, basal-plane defects, and S vacancies, which facilitate oxygen adsorption and activation[7–9]. The high specific surface area of 2D $MoS_2$ also

[1]Department of Applied Science and Technology, Politecnico di Torino, Torino, Italy. [2]Department of Chemical Sciences, University of Padova, Padova, Italy. [3]Materials and Processes Simulation Lab, Centre of New Technologies, University of Warsaw, Warsaw, Poland. [4]Center for Materials Research, Justus Liebig University, Giessen, Germany. [5]Nanotechnology Centre, Centre for Energy and Environmental Technologies (CEET), VSB–Technical University of Ostrava, Ostrava-Poruba, Czech Republic. [6]CNR Institute on Membrane Technology "Enrico Drioli", Unit of Padova, Padova, Italy. [7]Center for Sustainable Future Technologies @Polito, Istituto Italiano di Tecnologia, Torino, Italy. ✉e-mail: mengjiao.wang@polito.it; enzo.menna@unipd.it; teresa.gatti@polito.it

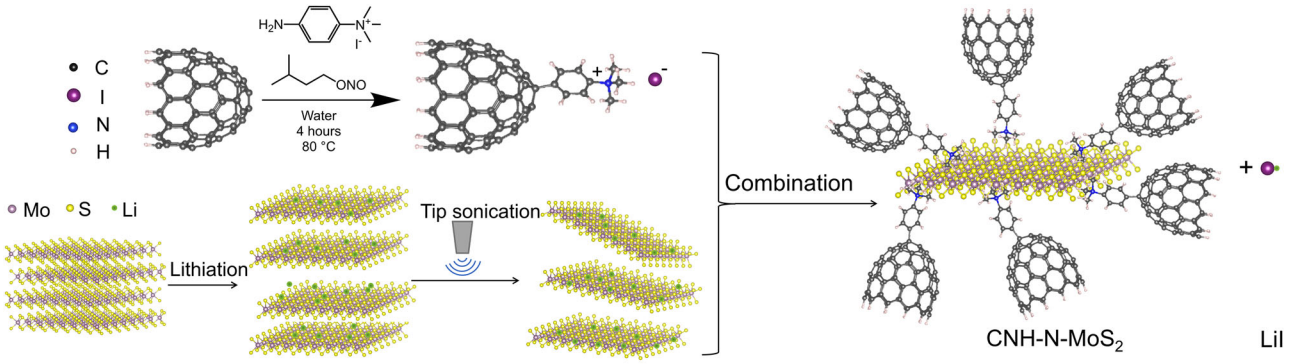



**Fig. 1 | Schematic illustration of the synthesis of CNH-N-$MoS_2$.** The scheme depicts the preparation of CNH-N, the exfoliation of layered $MoS_2$, and their subsequent assembly to form CNH-N-$MoS_2$. Pristine CNHs are first functionalized with TMA to obtain CNH-N, while bulk $MoS_2$ is exfoliated into thinner $MoS_2$ nanosheets by sonication. CNH-N and exfoliated $MoS_2$ nanosheets are then combined to promote interfacial interaction and formation of the CNH-N-$MoS_2$ hybrid structure, in which the functionalized groups are anchored to the $MoS_2$ surface. In the structural models, gray, rose red, blue, purple, yellow, green and pink spheres represent C, I, N, Mo, S, Li, and H atoms, respectively.

promotes mass transport and maximizes active-site exposure, while the metallic 1 T phase exhibits enhanced electrical conductivity and accelerated charge-transfer kinetics compared with the semiconducting 2H phase[10]. Accordingly, the electrocatalytic properties can be tailored through doping, phase engineering, and heterostructure construction to optimize the adsorption energies of ORR intermediates and increase the number of active sites[11,12]. For example, dopant engineering with Nb and Ta has been investigated, although these p-type dopants were found to negatively affect ORR activity[13]. In contrast, phase-engineered 1T/2H-$MoS_2$ exhibits superior performance owing to its improved conductivity and larger BET surface area, while hybrid systems combining $MoS_2$ with noble metals, Fe-based compounds, or Ni-based compounds have demonstrated enhanced activity and selectivity[14–17]. Despite these advances, the ORR performance of $MoS_2$ remains strongly dependent on catalyst design, and further improvements in activity, selectivity, and durability require a deeper understanding of the structure–property–activity relationships governing the reaction.

One particularly attractive strategy involves coupling $MoS_2$ with conductive carbon materials to exploit synergistic effects that improve electron transport, active-site utilization, and structural stability while avoiding the use of expensive or potentially hazardous components[18,19]. For example, abundant active sites of N-$MoS_2$/C derived from rich defects can enhance ORR activity, while the porous C is in charge of reducing catalyst aggregation[20]. $MoS_2$/reduced graphene oxide (rGO) has been employed as a catalyst or a platform for incorporating additional catalytic species such as Ni-based compounds[21,22]. The incorporation of electroactive N-doped graphene quantum dots into $MoS_2$/rGO nanohybrids further enhances ORR performance through favorable interfacial interactions and increased surface area and porosity[23]. Similarly, nitrogen-doped porous carbon sheets have been used to support $MoS_2$/SnS heterostructures, where the conductive carbon framework improves electron transfer and prevents catalyst agglomeration[24]. These studies clearly demonstrate the benefits of integrating $MoS_2$ with conductive carbon architectures.

Despite the above-mentioned carbon nanomaterials, carbon nanohorns (CNHs) have recently emerged as particularly promising building blocks for electrocatalytic applications[25]. CNHs are unique $sp^2$-hybridized carbon nanostructures composed of horn-shaped graphene tubules that self-assemble into spherical aggregates. In contrast to carbon nanotubes, whose functionalization often requires harsh chemical treatments, CNHs possess highly reactive five-membered-ring defects at their horn tips that facilitate efficient and homogeneous covalent modification. Moreover, their intrinsically porous three-dimensional architecture provides a large accessible surface area, efficient mass transport pathways, excellent electrical conductivity, and high chemical stability[26]. Recent advances in covalent chemistry have enabled the attachment of a variety of organic functionalities to CNHs, significantly improving their processability and expanding their application scope[27]. Nevertheless, examples of CNH-based hybrids with catalytically active nanostructures remain scarce. In particular, the integration of CNHs with TMDCs has received very limited attention, despite the complementary properties of these materials. While TMDCs offer abundant electrocatalytically active sites, they often suffer from limited conductivity, weak interfacial interactions, and structural restacking. The construction of CNH–TMDC heterostructures capable of efficiently catalyzing ORR therefore remains largely unexplored.

Motivated by these considerations, we envisioned that integrating metallic-phase 1T-$MoS_2$ nanosheets with the highly conductive and porous CNH framework could yield a robust 3D–2D heterostructure capable of efficiently catalyzing the four-electron ORR pathway toward $H_2O$. A critical aspect in the design of such CNH–$MoS_2$ electrocatalysts is the establishment of strong interfacial interactions between the two nanostructured components. Since neither pristine CNHs nor $MoS_2$ possess a sufficient density of dangling bonds for direct coupling, the introduction of suitable molecular linkers carrying complementary functionalities is required. In particular, the negatively charged exfoliated 1T-$MoS_2$ nanosheets necessitate a linker that can simultaneously interact with the π-conjugated surface of CNHs and provide positively charged functionalities capable of electrostatic association with $MoS_2$. Moreover, van der Waals and electrostatic interactions are expected to provide superior interfacial stability compared with weak van der Waals or supramolecular forces while simultaneously perturbing the electronic structure of the heterointerface, thereby influencing its electrocatalytic properties. Herein, we report the fabrication of a CNH–N–$MoS_2$ heterostructure through the functionalization of CNHs with 4-amino-N,N,N-trimethylbenzenaminium (TMA), which is covalently attached to the CNH surface and subsequently serves as an electrostatic anchor for negatively charged $MoS_2$ nanosheets (Fig. 1). The successive functionalization and assembly steps were systematically verified by thermogravimetric analysis (TGA), Raman spectroscopy, and transmission electron microscopy (TEM). The electrocatalytic activity of the resulting CNH–N–$MoS_2$ nanoconjugates toward ORR was then evaluated as a proof of concept. The results demonstrate that higher $MoS_2$ loadings lead to enhanced ORR performance, while the covalent attachment of TMA to CNHs and the electrostatic and van der Waals interactions with $MoS_2$ facilitate charge transfer across the heterointerface and increase the accessible catalytic surface area. As a result, the CNH–N–$MoS_2$ heterostructure exhibits excellent ORR selectivity, reaching 94%, highlighting the potential of engineered carbon–TMDC heterostructures for fuel-cell applications. Furthermore, density functional theory (DFT) calculations reveal that CNH functionalization induces electron-density redistribution within $MoS_2$ and that S sites located at the interface of metallic 1T-$MoS_2$ favor the four-

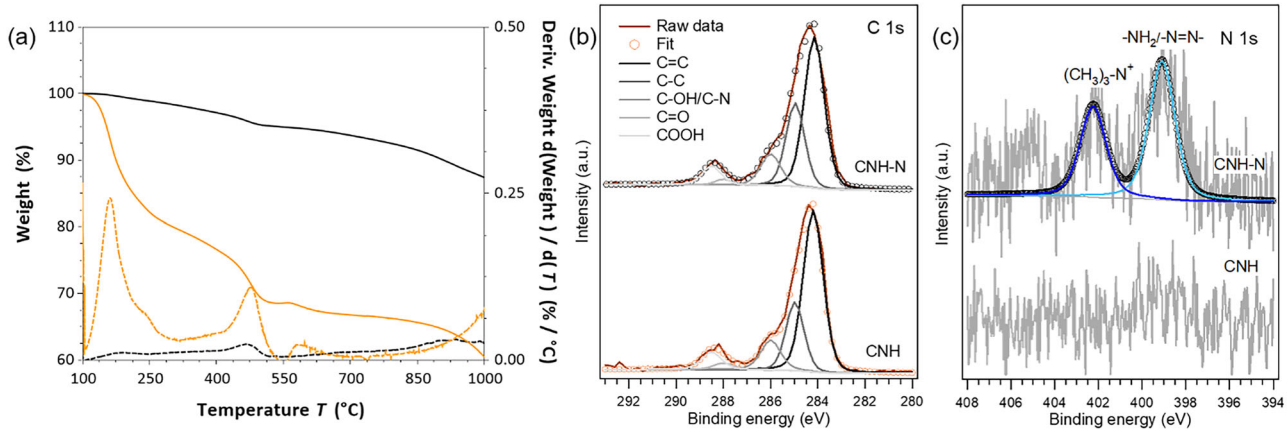



**Fig. 2 | Thermal and surface chemical characterization of CNH and CNH-N.** **a** TGA of CNHs (black lines) and CNH-N (yellow lines). The solid lines represent the weight loss as a function of temperature, while the dashed lines represent the corresponding DTG curves. **b** High-resolution C 1 s XPS spectra of CNH and CNH-N, together with the corresponding peak deconvolution. The orange open circles represent the experimental data, the orange solid lines represent the overall fitted envelopes, and the gray curves represent the individual fitted components. **c** High-resolution N 1s XPS spectra of CNH and CNH-N. The gray curves represent the experimental spectra, while the colored curves represent the fitted N 1 s components. The components assigned to quaternary ammonium nitrogen, $(CH_3)_3N^+$, and $NH_2$-/N=N-containing nitrogen species are indicated in the figure.

electron ORR pathway, providing mechanistic insight into the origin of the enhanced catalytic activity.

## Results

### Structural characterization

Functionalized CNH-N were synthesized through a diazotization reaction (Fig. 1) based on an adapted Tour functionalization protocol, which has previously been employed to prepare soluble derivatives of various carbon nanostructures[28–30]. The aniline precursor, TMA iodide, was synthesized according to a reported literature procedure[31]. Due to the hydrophilicity of covalently bonded TMA, CNH-N exhibited excellent water dispersibility, reaching 1.431 mg $mL^{-1}$, whereas stable aqueous suspensions of pristine CNHs could not be obtained. The presence of charged ammonium groups is expected to enhance interactions with water while suppressing hydrophobic and π–π stacking interactions between neighboring CNHs, thereby increasing colloidal stability. The optical images in Fig. S1 compare the aqueous dispersions of CNH and CNH-N. Following surface functionalization, CNH-N displays markedly improved hydrophilicity and enhanced colloidal stability relative to pristine CNHs. CNH-N and exfoliated 1T-$MoS_2$ were subsequently mixed at a weight ratio of 10:1, resulting in the formation of the CNH-N–$MoS_2$ hybrid via electrostatic and van der Waals interactions.

To confirm the successful surface functionalization, thermogravimetric analysis (TGA) was performed on both pristine CNHs and functionalized CNH-N samples. The thermal stability of the materials was evaluated under a nitrogen atmosphere (Fig. 2a). Pristine CNHs exhibited excellent thermal stability, showing only 5.30% weight loss between 100 and 600 °C, which could be attributed to the decomposition of oxygen-containing groups derived from the manufacturing process or residual solvent molecules. In contrast, CNH-N displayed a significantly higher weight loss of 32.09% within the same temperature range, indicating the presence of additional thermally labile functionalities introduced during the functionalization process. Specifically, TGA/derivative thermogravimetric (DTG) profiles of CNH-N reveal a two-step degradation behavior. The first weight-loss stage, occurring below 200 °C, is associated with the removal of physically adsorbed moisture and residual volatile species. The second degradation stage, centred at approximately 480 °C, is attributed to the thermal decomposition of grafted organic moieties and surface functional groups[31]. Beyond 550 °C, CNH-N exhibited remarkable thermal stability, retaining approximately 60% of its initial mass at 1000 °C, which reflects the presence of a highly stable carbonaceous framework. The substantially greater mass loss observed for CNH-N compared with pristine CNHs is attributed to the decomposition of covalently attached organic functionalities. These results provide strong evidence for the successful functionalization of the CNH. Although thermogravimetric analysis alone cannot distinguish covalent grafting from strongly adsorbed species, the substantial increase in the grafted organic fraction, together with the XPS and Raman results discussed below, consistently supports covalent attachment of TMA-derived aryl groups to the CNH framework, in agreement with previous reports on diazonium-functionalized CNHs[32].

**Table 1 | Quantification of the fitting peaks from C 1 s spectra of CNH, CNH-N and CNH-N-$MoS_2$**

| Sample | C=C(C sp2) | C-C (C sp3) | C-OH/C-N | C=O | COOH |
|---|---|---|---|---|---|
| CNH | 57.2% | 21.9% | 11.5% | 2.6% | 6.8% |
| CNH-N | 52.9% | 27.1% | 11.5% | 1.8% | 6.7% |
| CNH-N-$MoS_2$ | 59.4% | 19.0% | 10.43% | 2.6% | 8.6% |

To gain further insight into the surface chemical composition and the nature of the introduced functional groups, X-ray photoelectron spectroscopy (XPS) analysis was performed on pristine CNHs and CNH-N samples (Fig. 2b, c). The analysis of the C 1 s region of CNHs and CNH-N shows a main peak at 284.2 eV attributed to C $sp^2$ and a small component at 285.0 eV related to C $sp^3$ (Fig. 2b). In addition, weak peaks ascribed to oxygenated groups are detected, such as alcoholic (286.0 eV), carbonyl (287.9 eV), and carboxylic (288.9 eV) groups. Quantification of the C 1 s peaks showed an increase in the $sp^3$ carbon contribution from 21.9% to 27.9% and a corresponding decrease in the $sp^2$ carbon contribution from 57.2% to 52.9%, indicating that functionalization increased the density of $sp^3$ defects while partially disrupting the $sp^2$ carbon framework (Table 1). The analysis of the N 1 s region confirms the CNH modification as CNH-N, showing the expected $(CH_3)_3$–$N^+$ component at 402.4 eV (Fig. 2c). In addition, another component at 399.2 eV is observed, which could be attributed to –N = N– moieties. These azobenzene groups may be generated during the functionalization process either through diazo coupling between diazonium salts and surface-bound N,N,N-trimethylbenzylammonium groups, or via the radical decomposition of diazoanhydride intermediates formed during the Tour reaction mechanism[30]. It cannot be excluded that a small presence of -$NH_2$ species from residual aniline overlaps with the –N=N– signal. The appearance of nitrogen-containing species alone does not unequivocally distinguish covalent grafting from adsorption. However, the simultaneous

increase in the $sp^3$ carbon contribution (from 21.9 to 27.9%) indicates partial rehybridization of the graphitic lattice, which is expected following aryl radical addition through the diazonium reaction. This interpretation is independently corroborated by Raman spectroscopy, as discussed below. An additional weak signal at approximately 405 eV was also observed. This high-binding-energy component is attributed to oxidized nitrogen species ($NO_x$), which are likely formed through partial oxidation of nitrogen-containing surface groups during synthesis, purification, or subsequent exposure to air[33].

Dynamic light scattering (DLS) and ζ-potential measurements were performed to evaluate the colloidal properties of CNH-N and exfoliated 1T-MoS2 and to assess the feasibility of electrostatic assembly between the two components. The aqueous dispersion of CNH-N exhibited a hydrodynamic diameter of 126.1 nm, indicating good dispersion of the functionalized carbon nanohorns and showing good agreement with previously reported values[32,34,35]. The corresponding polydispersity index (PdI) of 0.143 suggests a relatively narrow particle-size distribution. Further evidence for the successful functionalization of CNHs was provided by ζ-potential measurements, which revealed a value of +36.9 mV. The positive value of ζ potential is associated with the presence of positively charged surface-bound quaternary ammonium groups, introduced during the functionalization process, and indicates good colloidal stability of the dispersion[30]. To obtain a complementary negatively charged counterpart for electrostatic assembly, bulk $MoS_2$ was exfoliated via lithium intercalation using *n*-butyllithium, followed by hydration and ultrasonic dispersion in water, as previously reported by us[36,37]. This procedure yielded exfoliated 1T-$MoS_2$ nanosheets with a strongly negative surface charge, as confirmed by a ζ-potential value of approximately −40 mV. The substantial difference in surface charge between CNH-N and 1T-$MoS_2$ promotes strong electrostatic attraction, facilitating the spontaneous assembly and stabilization of the CNH-N–$MoS_2$ hybrid material (Fig. 1). Therefore, the combination of covalent functionalization of CNHs and electrostatic self-assembly with negatively charged 1T-$MoS_2$ nanosheets represents an effective and versatile strategy for the fabrication of robust carbon–TMDC heterostructures.

Raman spectroscopy and XPS spectroscopy were employed to further verify the successful functionalization of CNHs and to investigate the van der Waals interaction between CNH-N and $MoS_2$. Measurements were performed using an excitation wavelength of 518 nm, which is resonant with the A-exciton transition of $MoS_2$. To minimize sample heating and avoid laser-induced damage, the laser power was limited to 0.3 mW $cm^{-2}$ and the exposure time was set to 10 s. The Raman spectra of pristine CNHs and CNH-N exhibit three characteristic features: the D band at approximately 1319 $cm^{-1}$, arising from disorder-induced vibrations associated with $sp^3$ defects in the carbon framework; the G band at approximately 1590 $cm^{-1}$, corresponding to the in-plane vibrational mode of $sp^2$-hybridized carbon atoms; and the second-order 2D band located at around 2678 $cm^{-1}$. The intensity ratio between the D and G bands ($I_D/I_G$) is commonly used to evaluate the degree of structural disorder and the density of $sp^3$ defects in carbon nanomaterials. For pristine CNHs, an $I_D/I_G$ ratio of 1.22 ± 0.05 was obtained, whereas CNH-N exhibited an increased ratio of 1.60 ± 0.20. This increase indicates the introduction of additional $sp^3$ defects. Within the graphitic framework, consistent with covalent aryl functionalization through the diazonium reaction. When considered together with the increase in the XPS $sp^3$ carbon contribution and the incorporation of nitrogen detected by XPS, these observations provide mutually consistent evidence for covalent surface grafting rather than simple adsorption of the TMA precursor. The relatively moderate increase in $I_D/I_G$ suggests that, although covalent bonds are formed on the CNH surface, the overall graphitic framework remains largely preserved[32,35]. Upon assembly with $MoS_2$, the $I_D/I_G$ ratio decreased to approximately 1.15. This behavior may be attributed to the passivation of pristine defect sites on the CNH surface by chemically introduced $MoS_2$. Exfoliated $MoS_2$ may preferentially interact with the defect sites on the CNH surface, effectively saturating these defects and thereby reducing the D-band intensity[38]. The observed decrease in the D-band signal suggests that the interaction between CNH-N and $MoS_2$ is not limited to simple electrostatic attraction but may also involve stronger interfacial electronic coupling between the two components. Similar reductions in Raman defect-related intensity ratios have been reported in carbon-based hybrid materials, where charge transfer and interfacial chemical interactions modify the electronic structure and Raman scattering response of the carbon phase. Therefore, the observed decrease in $I_D/I_G$ is consistent with the formation of a strongly electronically coupled CNH-N–$MoS_2$ heterostructure. The C 1 s XPS spectrum of CNH–N–$MoS_2$ (Fig. 3b) and the corresponding peak quantification reveal a decrease in $sp^3$-defect carbon to 19.0% and an increase in $sp^2$ carbon to 59.4% compared with CNH–N, consistent with the Raman results shown in Fig. 3a and Table 1. The relative contributions of the other characteristic peaks from C 1 s spectrum remain largely unchanged. Following coupling with $MoS_2$, the N 1 s envelope was redistributed toward lower binding energy, and the contribution from $(CH_3)_3–N^+$ was barely clearly resolved (Fig. S2). A remaining N-related contribution near 397.5 eV may indicate increased electronic screening of the nitrogen functionalities and therefore interfacial electronic coupling between CNH-N and $MoS_2$. However, the N 1 s region of the composite overlaps with Mo 3p3/2 contributions from the $MoS_2$[39]. Consequently, the strong feature around 397–400 eV cannot be assigned exclusively to N, and its apparent shift should not be interpreted as direct conversion of -$NH_2$/–N=N–. The reduced intensity of the 402–404 eV contribution is instead consistent with attenuation or reduced surface exposure after $MoS_2$ incorporation.

To further investigate the spatial distribution of these interactions, Raman mapping was performed over a 25 μm × 25 μm region of the CNH-N–$MoS_2$ hybrid (Fig. 3b, c). As shown in Fig. 3b, $MoS_2$-rich regions overlap preferentially with the edges of CNH-N aggregates. Correspondingly, the Raman map of the $I_D/I_G$ ratio reveals values close to 1.15 in these overlapping regions, represented by the green areas. In contrast, isolated red domains within the CNH-N aggregates exhibit $I_D/I_G$ values approaching 1.5, similar to those observed for the pristine CNH-N sample. These regions are attributed to CNH-N domains that are not in direct contact with $MoS_2$ nanosheets and therefore retain their original Raman characteristics. The spatial correlation between $MoS_2$ distribution and the decrease in the $I_D/I_G$ ratio provides strong evidence for interfacial interactions between the two components. The Raman mapping results therefore support the successful assembly of the CNH-N–$MoS_2$ hybrid and suggest the presence of charge-transfer or chemical coupling effects at the CNH-N/$MoS_2$ interface.

Overall, the combination of (i) the substantial grafted organic fraction measured by TGA, (ii) the appearance of the expected nitrogen species in XPS, (iii) the increase in the $sp^3$ carbon contribution in the C 1s spectrum, (iv) the increase in the Raman $I_D/I_G$ ratio indicating lattice rehybridization, and (v) the pronounced change in surface charge and dispersibility constitutes a coherent body of evidence supporting successful covalent functionalization of the CNH surface. This approach is consistent with the characterization generally adopted for diazonium-functionalized carbon nanohorns reported in the literature[32].

As to the characterization of 1T-$MoS_2$, the characteristic Raman signals of the 1 T phase are not distinguishable in the full Raman spectrum of the CNH-N–$MoS_2$ heterostructure because the Raman response is dominated by the high content of CNH-N (1:10 weight ratio of 1T-$MoS_2$ to CNH-N) (Fig. S3a). Similarly, no detectable Mo signal was observed in the XPS spectrum of the heterostructure (Fig. S4), which is also attributed to the low $MoS_2$ loading. To verify that the experimental procedures did not induce a phase transformation of 1T-$MoS_2$, pure 1T-$MoS_2$ was subjected to the same treatment, including dispersion in water for 20 h followed by centrifugation at 5000 rpm for 5 min. As shown in Fig. S3b, the characteristic $J_1$, $J_2$, and $J_3$ vibrational modes of the 1 T phase are clearly observed at approximately 155, 228, and 330 $cm^{-1}$, respectively, confirming that the 1T phase is retained after the treatment[40]. In addition, Raman peaks at approximately 288, 383, 407, and 451 $cm^{-1}$ are assigned to the 2H phase of $MoS_2$. The coexistence of the 1T and 2H phases is expected, as chemically exfoliated 1T-$MoS_2$ obtained by lithium intercalation is typically not phase-pure and

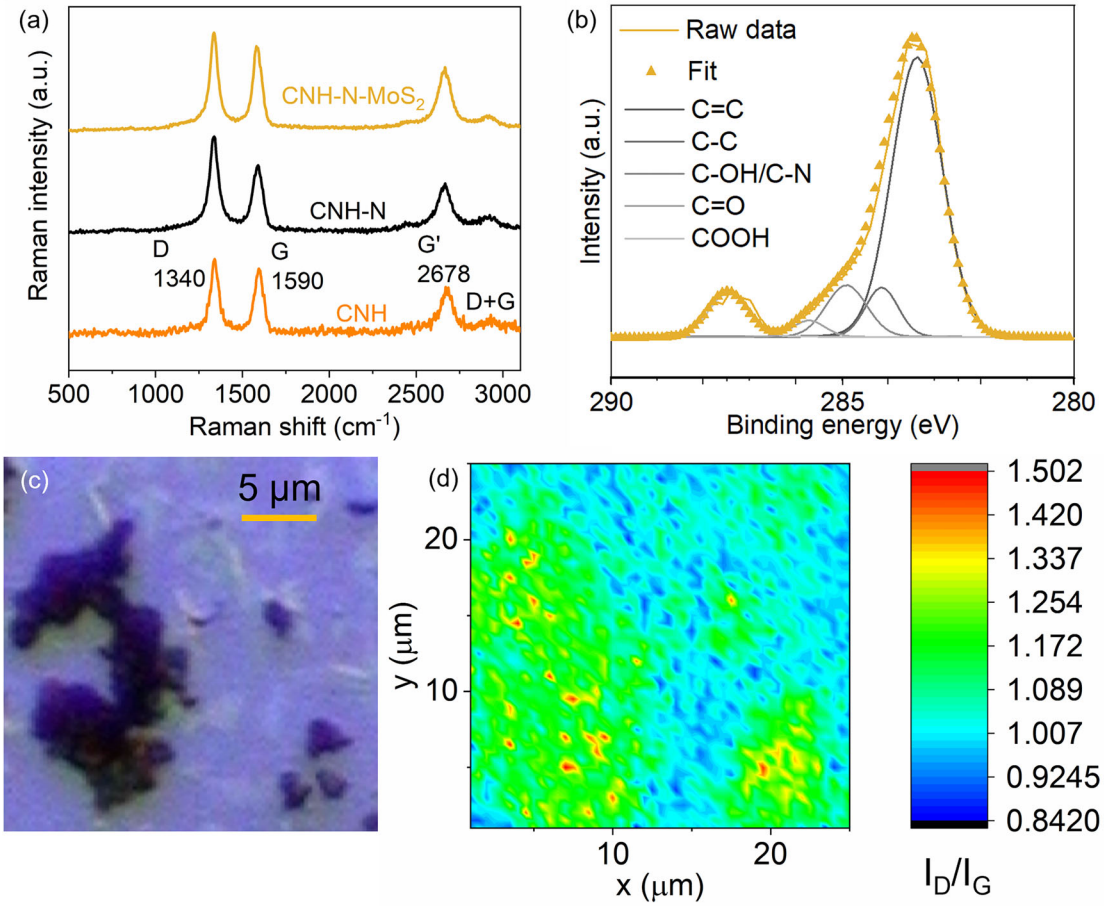



**Fig. 3 | Raman, XPS characterization and spatial Raman mapping of CNH-N-$MoS_2$.** **a** Raman spectra of CNHs (orange line), CNH-N (black line), and CNH-N-$MoS_2$ (yellow line). The characteristic D and G bands of the carbon framework are located at approximately 1340 and 1590 $cm^{-1}$, respectively, while the G′ band appears at approximately 2678 $cm^{-1}$. **b** High-resolution C 1 s XPS spectrum of CNH-N-$MoS_2$ and the corresponding peak deconvolution. The yellow solid line represents the raw experimental data, the yellow triangles represent the overall fit, and the individual fitted components are assigned to C=C, C–C, C–OH/C–N, C=O, and COOH species, as indicated by the black and gray curves. **c** Optical microscopy image of the CNH-N-$MoS_2$ region selected for Raman mapping; the scale bar corresponds to 5 μm. **d** Raman mapping of the intensity ratio between the D and G bands, $I_D/I_G$, over the selected region shown in panel (**c**). The color scale represents the spatial variation of $I_D/I_G$, increasing from blue for lower values to red for higher values, with values ranging from approximately 0.842 to 1.502.

invariably contains a certain fraction of the thermodynamically stable 2H phase[36].

The morphology, structure, and elemental composition of the synthesized nanostructures were investigated by a combination of TEM techniques, enabling analysis at the sub-nanometer scale (Fig. 4). Representative TEM images of CNH-N are shown in Figs. 4a, b, revealing spherical aggregates with diameters of approximately 50 nm. Notably, the outer edges of the CNHs are surrounded by a thin amorphous layer, which can be attributed to the presence of grafted TMA moieties on the CNH surface (Fig. 4b). Following hybridization, large exfoliated $MoS_2$ nanosheets with lateral dimensions of ~500 nm were observed to be decorated by and intimately associated with CNH-N aggregates (Fig. 4c). A higher-magnification image of the selected region (Fig. S5) clearly demonstrates the close contact between CNH-N and $MoS_2$, indicating successful assembly of the heterostructure. Selected regions in Fig. 4d are enlarged in Fig. 4e, f to highlight the atomic structures of the 1T and 2H phases, respectively. The 1T phase exhibits the characteristic octahedral coordination of Mo atoms, in which the individual S atoms show reduced contrast (Fig. 4e). In contrast, the 2H phase displays the expected hexagonal arrangement with clearly resolved Mo and S atomic columns (Fig. 4f). The corresponding lattice fringes, with spacings of approximately 0.27 nm for 1T-$MoS_2$ and 0.31 nm for 2H-$MoS_2$, are consistent with the respective crystallographic planes of the two phases, further supporting the phase identification[41]. This result is consistent with the Raman spectra (Fig. S3b), confirming that the synthesized 1T-$MoS_2$ is not phase-pure and contains a certain proportion of the 2H phase. Finally, the elemental distribution obtained by energy-dispersive X-ray spectroscopy (EDS) mapping (Fig. 4g) confirms the coexistence of carbon, molybdenum, and S within the same nanostructure, providing direct evidence for the successful integration of CNH-N and $MoS_2$ into the hybrid material.

### Electrocatalytic ORR

Cyclic voltammetry (CV) measurements were first performed in $O_2$-saturated 0.1 M KOH solution to investigate the electrochemical behavior of the prepared materials (Fig. 5a). Pristine CNHs exhibited a noticeably higher capacitive current than CNH-N, suggesting that functionalization with TMA groups occupies a significant fraction of the electrochemically active defect sites and surface functionalities present on the CNH surface. But considering that the catalyst is the same, it is also possible that the actual weight of CNH in CNH-N is reduced, thus reducing the active sites. A similarly low capacitive current was observed for CNH-N–$MoS_2$, indicating that the surface properties of CNH-N are largely retained after hybrid formation. In contrast, the physical mixture of CNHs and $MoS_2$ displayed a capacitive response closer to that of pristine CNHs, consistent with the absence of covalent functionalization. All carbon-containing samples exhibited a redox feature centered at approximately 0.82 V vs. RHE. This

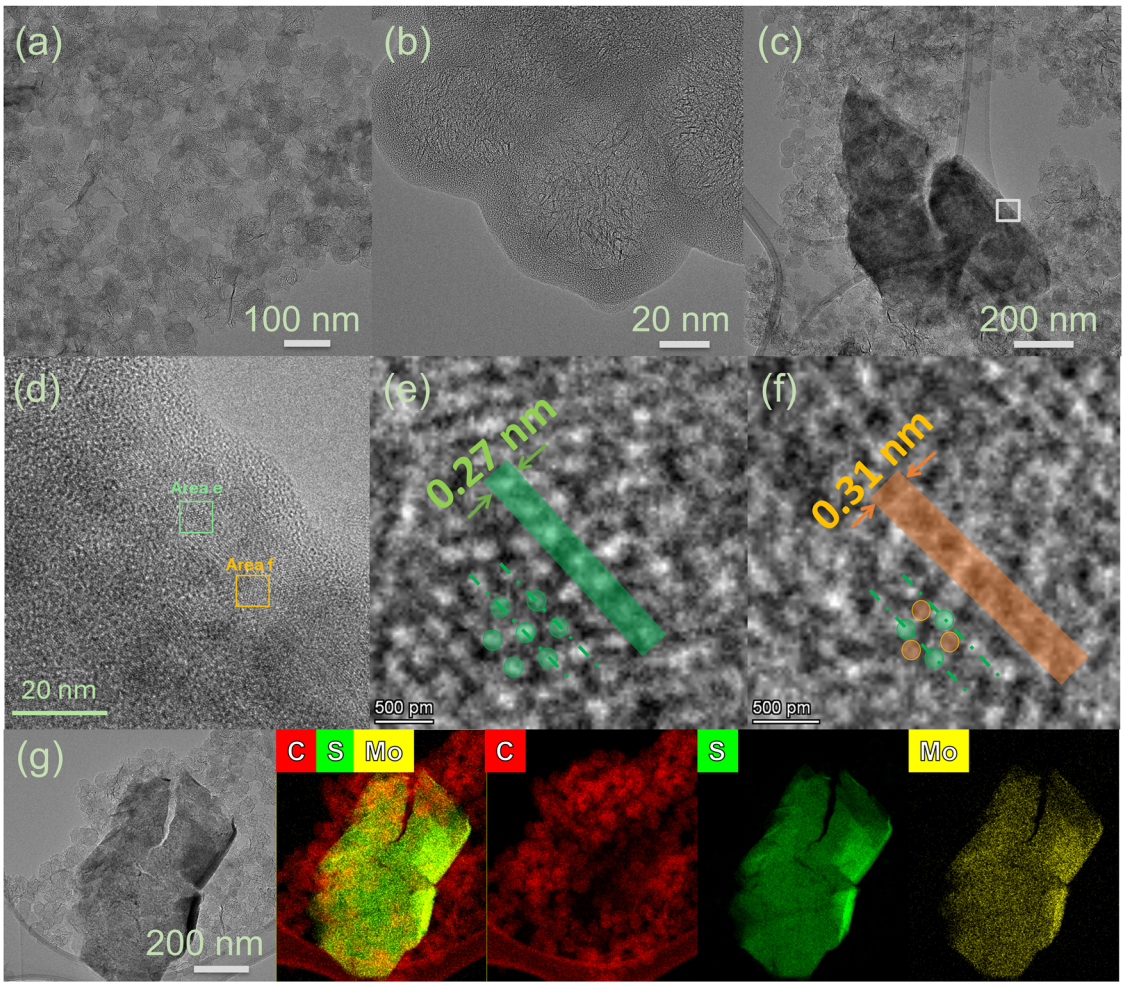



**Fig. 4 | Electron microscopy characterization of CNH-N and CNH-N-$MoS_2$.** **a**, **b** Low- and high-magnification TEM images, respectively, of CNH-N, showing the characteristic aggregated nanohorn morphology and graphitic structure. **c** TEM image of CNH-N-$MoS_2$; the white square indicates the region selected for high-resolution analysis. **d** High-resolution transmission electron microscopy (HRTEM) image acquired from the region marked by the white square in (**c**). The green and orange boxes indicate the regions further analyzed in (**e**) and (**f**), respectively. **e**, **f** Enlarged atomic-resolution images of the regions marked in panel (d), showing representative structures assigned to the 1T and 2H phases of $MoS_2$, respectively. 1 T and 2H denote the octahedrally and trigonal-prismatically coordinated polymorphs of $MoS_2$, respectively. The measured characteristic spacings are approximately 0.27 nm for the 1 T phase and 0.31 nm for the 2H phase. Green and orange overlays indicate the positions of Mo and S atoms, respectively. **g** Scanning transmission electron microscopy (STEM) image of a representative CNH-N-$MoS_2$ together with the corresponding elemental distribution maps, demonstrating the spatial distribution of C, S, and Mo. In the elemental maps, red represents C, green represents S, and yellow represents Mo; the merged map shows the spatial overlap of the three elements.

signal has previously been associated with doping-induced charge delocalization and modifications of the spin density distribution within the $sp^2$ carbon network, which facilitate oxygen adsorption and O=O bond activation[42]. The persistence of this feature after functionalization and hybridization suggests that these active carbon sites remain electrochemically accessible. Pure $MoS_2$ displayed a redox process at approximately 0.80 V, which is attributed to the formation of adsorbed Mo–OH species[43]. All samples exhibit a cathodic peak at approximately 0.5 V vs. RHE in $O_2$-saturated electrolyte without electrode rotation. The peak results from the transition from kinetically controlled to diffusion-limited ORR. As the potential shifts negatively, the ORR kinetics accelerate and the cathodic current increases. Once the rate of $O_2$ consumption exceeds the rate of $O_2$ diffusion from the bulk electrolyte, mass transport becomes limited, leading to a decrease in the current.

To evaluate the ORR activity, rotating disk electrode (RDE) measurements were performed (Fig. 5b). Pristine CNHs and CNH-N exhibited similar ORR onset potentials of approximately 0.72 V vs. RHE, indicating that surface functionalization alone does not significantly alter the ORR onset. In contrast, the CNH-N–$MoS_2$ heterostructure showed a substantially improved onset potential of 0.80 V. Furthermore, CNH-N–$MoS_2$ achieved a half-wave potential of 0.74 V, highlighting its superior electrocatalytic performance. To prove the synergistic effect between CNH-N and $MoS_2$ in the hybrid material, thanks to the covalent functionalization and the electrostatic interactions, a physical mixture of CNHs and $MoS_2$ was prepared with the same $MoS_2$ content as in the hybrid material. As seen in Fig. 5b, the physical mixture exhibited an intermediate onset potential of 0.74 V, lying between those of pristine CNHs (0.72 V) and $MoS_2$ (0.77 V), which confirms the absence of any synergistic effect between the two in the absence of any interaction. To further evaluate the intrinsic catalytic activity, the electrochemically active surface area (ECSA) was estimated from the double-layer capacitance ($C_{dl}$) obtained from CV measurements in the non-Faradaic region. As shown in Fig. 5c, pristine CNHs exhibited the highest $C_{dl}$ (0.64 mF $cm^{-2}$), followed by CNH+$MoS_2$ (0.61 mF $cm^{-2}$), indicating that CNHs provide the largest electrochemically accessible surface area. The similar $C_{dl}$ values of CNHs and CNH+$MoS_2$ suggest that physically mixing $MoS_2$ with CNHs has little effect on the accessible surface area. In contrast, the functionalization of CNHs decreased the $C_{dl}$ to 0.43 mF $cm^{-2}$.

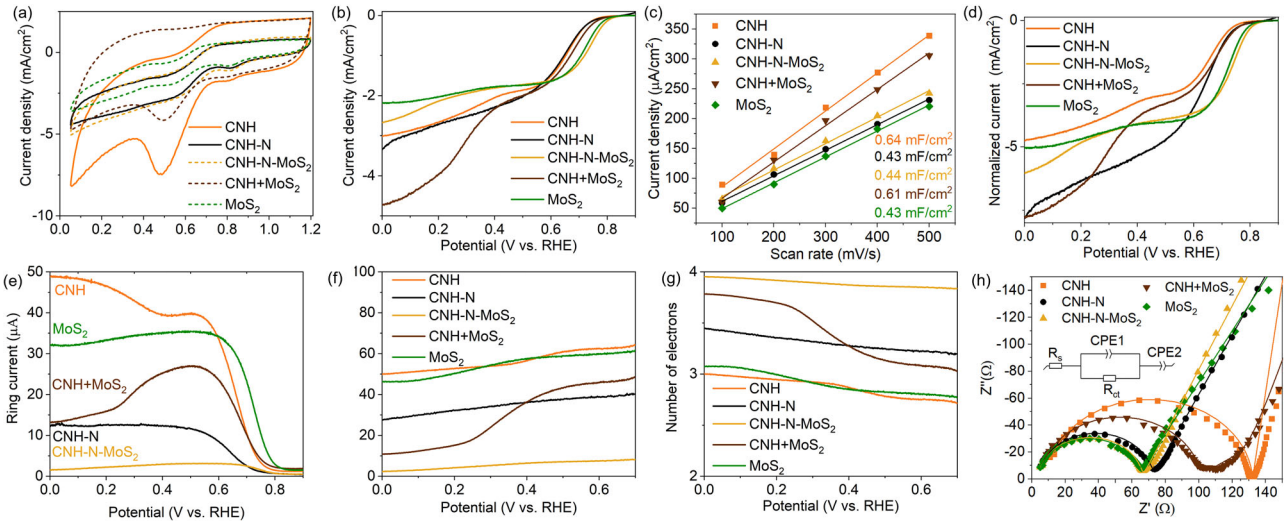



**Fig. 5 | Electrochemical ORR performance and impedance characteristics of CNH, CNH-N, CNH-N-$MoS_2$, CNH+$MoS_2$, and $MoS_2$.** **a** CV curves recorded in $O_2$-saturated 0.1 M KOH electrolyte. CNH, CNH-N, CNH-N-$MoS_2$, CNH+$MoS_2$, and $MoS_2$ are represented by orange, black, yellow, brown, and green curves, respectively. **b** RRDE measurements recorded in $O_2$-saturated 0.1 M KOH at a rotation rate of 1600 rpm. (**c**) Capacitive current density as a function of scan rate used to determine $C_{dl}$ of the different catalysts. Orange squares, black circles, yellow upward triangles, brown downward triangles, and green diamonds represent CNH, CNH-N, CNH-N-$MoS_2$, CNH+$MoS_2$, and $MoS_2$, respectively. The corresponding $C_{dl}$ values are indicated in the panel. **d** ECSA-normalized linear sweep voltammetry (LSV) curves of the catalysts. **e** Corresponding ring currents obtained from the RRDE measurements. **f** Potential-dependent selectivity toward hydroperoxide ($HO_2^-$) derived from the RRDE data. **g** Number of electrons transferred per oxygen molecule during the oxygen reduction reaction as a function of applied potential. **h** Nyquist plots obtained from EIS measurements of all catalysts. Orange squares, black circles, yellow upward triangles, brown downward triangles, and green diamonds represent the experimental data for CNH, CNH-N, CNH-N-$MoS_2$, CNH+$MoS_2$, and $MoS_2$, respectively, while the corresponding solid lines represent the fitted impedance spectra. The inset shows the equivalent circuit used for fitting, comprising the series resistance $R_s$, charge-transfer resistance $R_{ct}$, and constant-phase elements CPE1 and CPE2. Potentials are reported versus RHE.

CNH-N–$MoS_2$ (0.44 mF $cm^{-2}$) exhibited a $C_{dl}$ nearly identical to that of CNH-N (0.43 mF $cm^{-2}$) and pristine $MoS_2$ (0.43 mF $cm^{-2}$), indicating that the chemical growth of $MoS_2$ on CNH-N does not significantly alter the electrochemically accessible surface area. These observations are consistent with the trends observed in the CV curves shown in Fig. 5a. To eliminate the influence of ECSA, the ORR polarization curves were subsequently normalized by ECSA (Fig. 5d). After normalization, CNH-N retained a higher current density than pristine CNHs, indicating that N functionalization enhances the intrinsic activity of the catalytic sites rather than simply increasing the number of accessible active sites. CNH-N exhibited a higher cathodic current density than CNH-N–$MoS_2$ over most of the investigated potential range, indicating that the formation of the heterostructure does not significantly enhance the intrinsic ORR activity relative to $MoS_2$ on a per-active-area basis. In contrast, the ECSA-normalized polarization curve of CNH-N–$MoS_2$ more closely resembles that of $MoS_2$, particularly in terms of the ORR onset potential. The incorporation of $MoS_2$ therefore shifts the ORR onset of CNH-N toward more positive potentials, approaching that of $MoS_2$, suggesting that $MoS_2$-related sites play a dominant role in determining the onset of oxygen reduction. Notably, the physical CNH + $MoS_2$ mixture does not reproduce this behavior, highlighting the importance of the engineered CNH-N/$MoS_2$ interface rather than a simple additive contribution from the two components. Together with the results of selectivity in Fig. 5f, these observations suggest that $MoS_2$ provides the principal ORR-active sites for the four-electron reaction, while CNH-N acts as an electronically coupled conductive framework that facilitates interfacial charge transfer and promotes efficient utilization of the $MoS_2$ catalytic sites.

Besides catalytic activity, the ORR pathway is another critical parameter for evaluating electrocatalyst performance. In alkaline media, ORR can proceed either through a two-electron pathway producing peroxide species or through the preferred four-electron pathway directly generating hydroxide ions:

$$O_{2+}H_2O_{+}2e^- \rightarrow HO_2^- + OH^- \ (U^\circ = 0.76\ \text{V vs. RHE})$$

$$O_{2+}2H_2O_{+}4e^- \rightarrow 4OH^- \ (U^\circ = 1.23\ \text{V vs. RHE})$$

Because peroxide species can decrease energy efficiency and promote electrode degradation, minimizing their formation is highly desirable. Ring-disk measurements revealed that the ring current associated with peroxide generation was remarkably low for CNH-N–$MoS_2$, whereas substantially higher ring currents were observed for all other samples (Fig. 5c). This result indicates greatly suppressed peroxide formation on the heterostructure catalyst.

Quantitative analysis of the RRDE data further confirmed significant differences in the ORR mechanism (Fig. 5d, e). At 0.7 V vs. RHE, the number of electrons transferred (n) was approximately 3.8 for CNH-N–$MoS_2$, compared with 3.2 for CNH-N and 2.7–2.8 for pristine CNHs and $MoS_2$. These values correspond to peroxide yields of approximately 6%, 40%, 64%, and 61%, respectively. Therefore, ORR on CNH-N–$MoS_2$ proceeds predominantly through a quasi-four-electron pathway with minimal peroxide production, approaching the performance of commercial Pt/C reported in our previous work, where the measurements were carried out under identical experimental conditions[44]. In contrast, the individual components preferentially follow the less desirable two-electron pathway. The physical mixture of CNHs and $MoS_2$ exhibited an intermediate electron transfer number of approximately 3.3, demonstrating that simple mixing cannot reproduce the performance of the heterostructure. These results clearly indicate that the synergistic interaction established through covalent functionalization and electrostatic assembly is essential for promoting the selective four-electron ORR pathway. A comparison between the CNH-N–$MoS_2$ catalyst developed in this work and representative ORR catalysts

**Table 2 | Comparison with CNH-N–$MoS_2$ regarding onset potential, half-wave potential, and selectivity**

| Sample name | Onset potential | Half-wave potential | $H_2O_2$ yield | Ref. |
|---|---|---|---|---|
| 4-aminobenzoic acid functionalized carbon nanotubes | 0.81 V vs RHE | NR | 75.5% at 0.30 V | 56 |
| $MoS_2$@rGO | 0.90 V vs RHE | 0.78 V vs RHE | 0.45% over 0.40–1.00 V | 57 |
| FeTPP-functionalized carbon nanotubes | 0.79 V vs RHE | 0.64 V vs RHE | <5% at high overpotential | 58 |
| 2H 2D-$MoS_2$ | 0.16 V vs SCE | NR | NR | 6 |
| Pyridine-functionalized carbon nanotubes | −0.144 V vs Ag/AgCl/KCl (sat.) | NR | NR | 59 |
| $MoS_2$–Carbon Nanotube (1:4) | −0.35 V vs Ag/AgCl | ≈−0.275 V vs Ag/AgCl† | <10% over −0.8 to −0.4 V | 60 |
| FePc/Py-carbon nanotubes | ≈0.915 V vs RHE† | ≈0.86 V vs RHE† | NR | 61 |
| N-$MoS_2$/C | ≈0.20 V vs Ag/AgCl† | NR | NR | 20 |
| FeNi–$MoS_2$/rGO | 0.988 V vs RHE | 0.895 V vs RHE | NR | 21 |
| Ni/$MoS_2$-rGO | 0.86 V vs RHE | 0.74 V vs RHE | NR | 62 |
| [NO_PRINTED_FORM]Pyridine functionalized carbon nanotubes | 0.760 V vs RHE | ≈0.63 V vs RHE† | 45.6% at 0.50 V | 63 |
| N-GQDs/$MoS_2$-rGO | 0.81 V vs RHE | ≈0.61 V vs RHE† | ≈9–30% over 0–0.8 V | 64 |
| $MoS_2$/rGO | 0.97 V vs RHE | 0.83 V vs RHE | NR | 23 |
| CNH-N–$MoS_2$ | 0.8 V vs. RHE | 0.74 V vs. RHE | 2-8% over 0-0.7 V vs. RHE | Our work |

based on functionalized carbon materials and/or $MoS_2$ is presented in Table 2. The CNH-N–$MoS_2$ heterostructure exhibits onset and half-wave potentials comparable to those of previously reported catalysts. More importantly, it achieves one of the highest $H_2O$ selectivity during a wide range of potentials among the reported systems, highlighting its excellent preference for the four-electron ORR pathway. This high selectivity toward $H_2O$ production represents the key advantage of the present catalyst and constitutes the main contribution to this work.

Electrochemical impedance spectroscopy (EIS) was subsequently employed to investigate the interfacial charge-transfer properties of the catalysts (Fig. 5h). The equivalent circuit used to fit the impedance spectra is shown in the inset of Fig. 5h, and the fitted values of the series resistance ($R_s$) and charge-transfer resistance ($R_{ct}$) are summarized in Table S2. CNH-N, CNH-N–$MoS_2$, CNH+$MoS_2$, and $MoS_2$ exhibited relatively low Rs values, indicating good electrolyte and electrode conductivity[45]. In contrast, pristine CNHs showed a higher Rs of approximately 8 Ω, suggesting a relatively larger resistance associated with the electrode or interfacial contact. More importantly, the $R_{ct}$ decreased markedly from 123 Ω for pristine CNHs to 67 Ω for CNH-N and further to 62 Ω for CNH-N–$MoS_2$. Considering that pure 1T-$MoS_2$ exhibits an $R_{ct}$ of 59 Ω, the significantly reduced charge-transfer resistance of the heterostructure can be attributed to the combined effects of nitrogen functionalization and the intrinsically high electrical conductivity of 1T-$MoS_2$. The lower $R_{ct}$ demonstrates more efficient interfacial electron transfer, which is beneficial for accelerating the ORR kinetics. In contrast, the physical mixture of CNHs and $MoS_2$ retained a much higher $R_{ct}$ of 103 Ω, indicating that simple physical mixing does not effectively improve charge transport. These results demonstrate that nitrogen functionalization promotes stronger electronic coupling between CNHs and $MoS_2$, thereby facilitating interfacial charge transfer. The exponent of the first constant phase element (CPE1, n1) was close to unity for CNH, CNH-N, CNH-N–$MoS_2$, and $MoS_2$, indicating an approximately ideal capacitive response at high frequencies. In contrast, the lower n1 value of CNH+$MoS_2$ suggests a more heterogeneous electrode/electrolyte interface. The second constant phase element (CPE2, n2) describes a distributed low-frequency process, which is attributed to the combined effects of oxygen diffusion, ion transport within the porous electrode, and the relaxation of adsorbed ORR intermediates, rather than an additional discrete capacitive process. The stronger diffusion-related contribution observed for CNH +$MoS_2$ also explains the less satisfactory fitting of its low-frequency region using the common equivalent circuit. Overall, the substantially lower Rct and the better agreement with the common equivalent-circuit model for CNH-N–$MoS_2$, compared with the physically mixed CNH+$MoS_2$, provide strong evidence that nitrogen functionalization enables more effective electronic coupling at the CNH/$MoS_2$ interface, thereby enhancing charge-transfer kinetics during the ORR[46].

Concisely, the CNH-N–$MoS_2$ outperforms the CNH-N, $MoS_2$, and mixed CNH+$MoS_2$ counterparts during the ORR tests, in terms of both catalytic activity and 4-electron pathway selectivity. The enhanced ORR performance of CNH-N–$MoS_2$ is attributed to the intimate coupling between the two components through covalent attachment and interfacial van der Waals interactions. These interactions facilitate charge transfer across the heterointerface, as evidenced by a much lower charge transfer resistance. In addition, they are also expected to optimize the adsorption energies of ORR intermediates and consequently affect the reaction pathways.

### Stability test

The durability of CNH-N–$MoS_2$ was evaluated by chronoamperometry (CA) at 0.68 V vs. RHE in air-saturated electrolyte using Ti foil as the substrate. As shown in Fig. 6a, the catalyst retained approximately 75% of its initial current after prolonged operation, with commercial Pt/C reported as a benchmark in our previous work[44]. The post-CA electrode was subsequently characterized by Raman spectroscopy and XPS to assess its structural and chemical stability. As shown in Fig. 6b, the characteristic D and G bands of the CNHs remained clearly visible after CA, whereas the Raman modes of $MoS_2$ were still not detectable. This may be attributed to the relatively low initial $MoS_2$ loading, together with partial detachment or redistribution of the $MoS_2$ nanosheets during prolonged electrochemical operation. The $I_D/I_G$ ratio increased from approximately 1.15 for the as-prepared CNH-N–$MoS_2$ heterostructure to 1.65 after CA. This increase indicates greater structural disorder in the carbon framework and may result from the loss of $MoS_2$-induced defect passivation and/or electrochemical oxidation of the CNH surface. The absence of detectable $MoS_2$ Raman modes does not necessarily indicate its complete removal, particularly considering the lower sensitivity of Raman spectroscopy toward trace amounts of $MoS_2$ in the carbon-rich residue. Indeed, Mo and S signals were still detected by the more surface-sensitive XPS analysis. As shown in Fig. 6c, approximately 229.09 and 232.42 eV is assigned to $Mo^{4+}$ species characteristic of 2H $MoS_2$. A second doublet at approximately 229.80 and 233.07 eV is attributed to Mo atoms in a more electron-deficient local environment, likely associated with sulfur-deficient $MoS_{2-x}$ domains or partially oxidized Mo–O–S species. The higher-binding-energy doublet at approximately 230.36 and 233.58 eV is tentatively assigned to $Mo^{5+}$, indicating partial surface oxidation of the Mo-containing phase. No distinct low-binding-energy doublet characteristic of 1T-$MoS_2$ was detected. The fitted spin–orbit separations are slightly larger than the ideal value

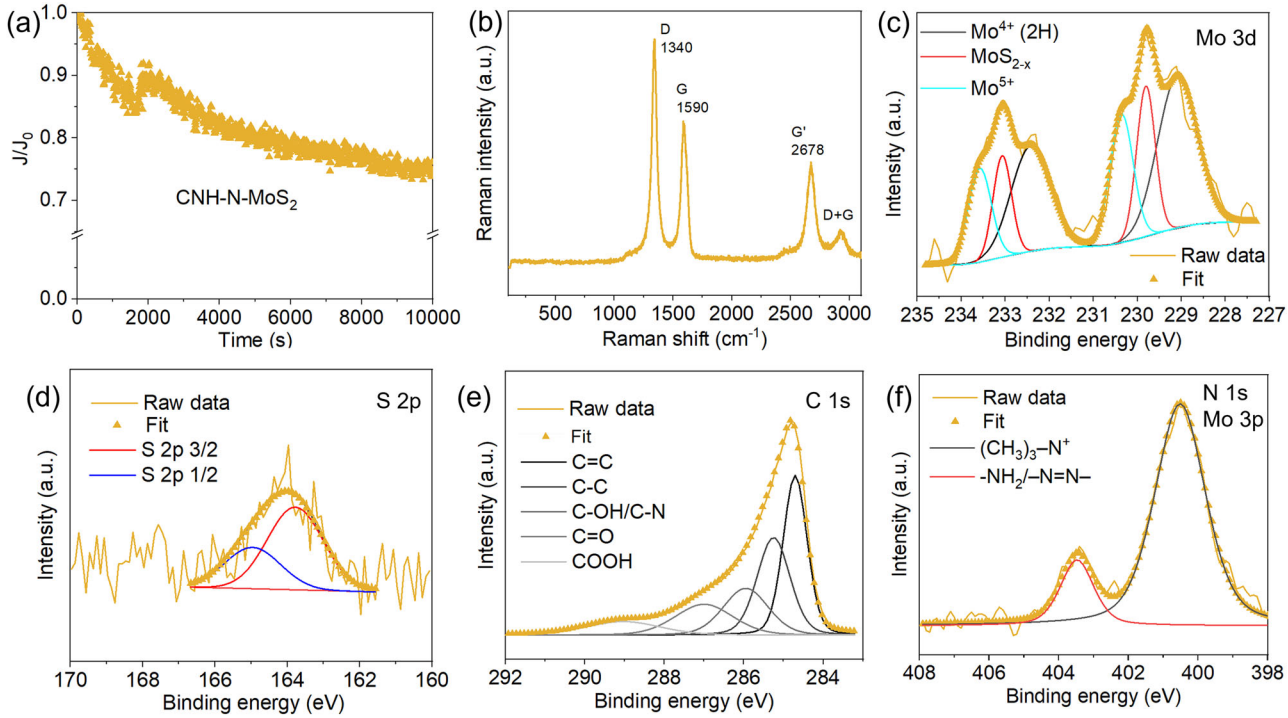



**Fig. 6 | Electrochemical durability and post-stability structural and surface chemical characterization of CNH-N-$MoS_2$.** **a** CA stability measurement of CNH-N-$MoS_2$ performed at 0.68 V vs. RHE. The normalized current density, expressed as J/J0, where J and J0 are the current density at a given time and the initial current density, respectively, is plotted as a function of time. Yellow triangles represent the experimental data. **b** Raman spectrum of CNH-N-$MoS_2$ collected after the CA measurement, showing the characteristic D, G, G′, and D + G bands of CNH at approximately 1340, 1590, 2678 $cm^{-1}$, and the corresponding higher-wavenumber region, respectively. **c** High-resolution Mo 3 d XPS spectrum of CNH-N-$MoS_2$ after CA and the corresponding peak deconvolution. The yellow solid line represents the raw experimental data, and the yellow triangles represent the overall fit. The black, red, and cyan curves correspond to $Mo^{4+}$ associated with the 2H-$MoS_2$ phase, $MoS_{2-x}$ species, and $Mo^{5+}$ species, respectively. **d** High-resolution S 2p XPS spectrum after CA. The yellow solid line and yellow triangles represent the raw data and overall fit, respectively, while the red and blue curves correspond to the S 2p3/2 and S 2p1/2 components, respectively. **e** High-resolution C 1 s XPS spectrum after CA and its peak deconvolution. The yellow solid line represents the raw data, the yellow triangles represent the overall fit, and the black and gray curves represent the individual components assigned to C=C, C–C, C–OH/C–N, C=O, and COOH species. **f** High-resolution N 1 s XPS region after CA. The yellow solid line and yellow triangles represent the raw data and overall fit, respectively. The gray and red components are assigned to quaternary ammonium nitrogen, $(CH_3)_3N^+$, and $NH_2$-/N = N-containing nitrogen species, respectively, while the contribution from the overlapping Mo 3p signal is also included in the fitting.

commonly reported for crystalline $MoS_2$. This deviation is likely caused by the strong overlap of multiple Mo chemical states, structural disorder, and the distribution of local bonding environments, which can shift the apparent peak positions in unconstrained fitting. The S 2p spectrum shows a doublet at 163.8 and 165.0 eV, corresponding to the S 2p3/2 and S 2p1/2 components, respectively. The spin–orbit splitting of approximately 1.2 eV is consistent with S 2p. Although these binding energies are higher than those typically reported for lattice $S^{2-}$ in stoichiometric 2H-$MoS_2$, they may originate from sulfur atoms in defective, edge-rich, or chemically modified 2H $MoS_2$ environments, including S–S or C–S bonding. The C 1 s spectrum contained contributions from C = C $sp^2$ carbon at approximately 284.5 eV, $sp^3$ C–C/C–H at 285.2 eV, overlapping C–O/C–N environments at 286.0 eV, carbonyl groups at 287.0 eV, and carboxylic groups at 289.0 eV (Fig. 6e). Following CA, the $sp^2$ carbon contribution decreased from 59.4% to 32.1%, whereas the $sp^3$ contribution increased from 19.0% to 26.9% (Table 3). The relative contributions of the oxygenated carbon components also increased. These changes are consistent with the higher Raman $I_D/I_G$ ratio and indicate increased structural disorder and partial oxidation or reconstruction of the CNH surface. The persistence of the N 1 s signal in Fig. 6f suggests that some nitrogen-containing TMA functionalities might remain in the recovered material, although part of the signal may originate from the overlapping Mo 3p contribution, as discussed previously for Fig. S2. Overall, CNH-N–$MoS_2$ retained a substantial fraction of its initial current and predominantly preserved the 1 T phase of the remaining $MoS_2$. Nevertheless, post-CA characterization revealed partial oxidation of $MoS_2$, disruption of the heterostructure, increased disorder and oxygenation of the carbon framework, and probable catalyst loss. The current decay is therefore attributed to a combination of chemical degradation at the CNH-N/$MoS_2$ interface and physical loss or delamination of the catalyst layer from the Ti substrate. Electrolyte screening of the electrostatic CNH-N/$MoS_2$ interaction may further weaken the heterointerface during prolonged polarization[44].

**Table 3 | Quantification of the fitting peaks from C 1 s spectra of CNH-N-$MoS_2$ after CA**

| Sample | C = C ($sp^2$) | C-C ($sp^3$) | C-OH/C-N | C = O | COOH |
|---|---|---|---|---|---|
| CNH-N-$MoS_2$ | 32.1% | 26.9% | 17.6% | 15.0% | 8.5% |

## Computational modeling studies

To understand the influence of functionalization of CNHs in ORR pathways, we performed DFT-based computations on both electronic and catalytic properties of the heterojunctions with and without functionalized TMA (Fig. 7a). The electronic structure analysis points to a clear strengthening of interfacial charge redistribution after functionalization. The interface formation is responsible for a transfer of electrons at the interface, from the CNH to the $MoS_2$ component. The TMA-modified CNH is more strongly adsorbed to the $MoS_2$ monolayer at a distance of 0.16 nm instead of 0.31 nm for pristine CNH (for more detail, see Fig. S6 in SI). Bader charge analysis allows us to quantify the electron transfer upon interface formation, confirming that the magnitude of this transfer is

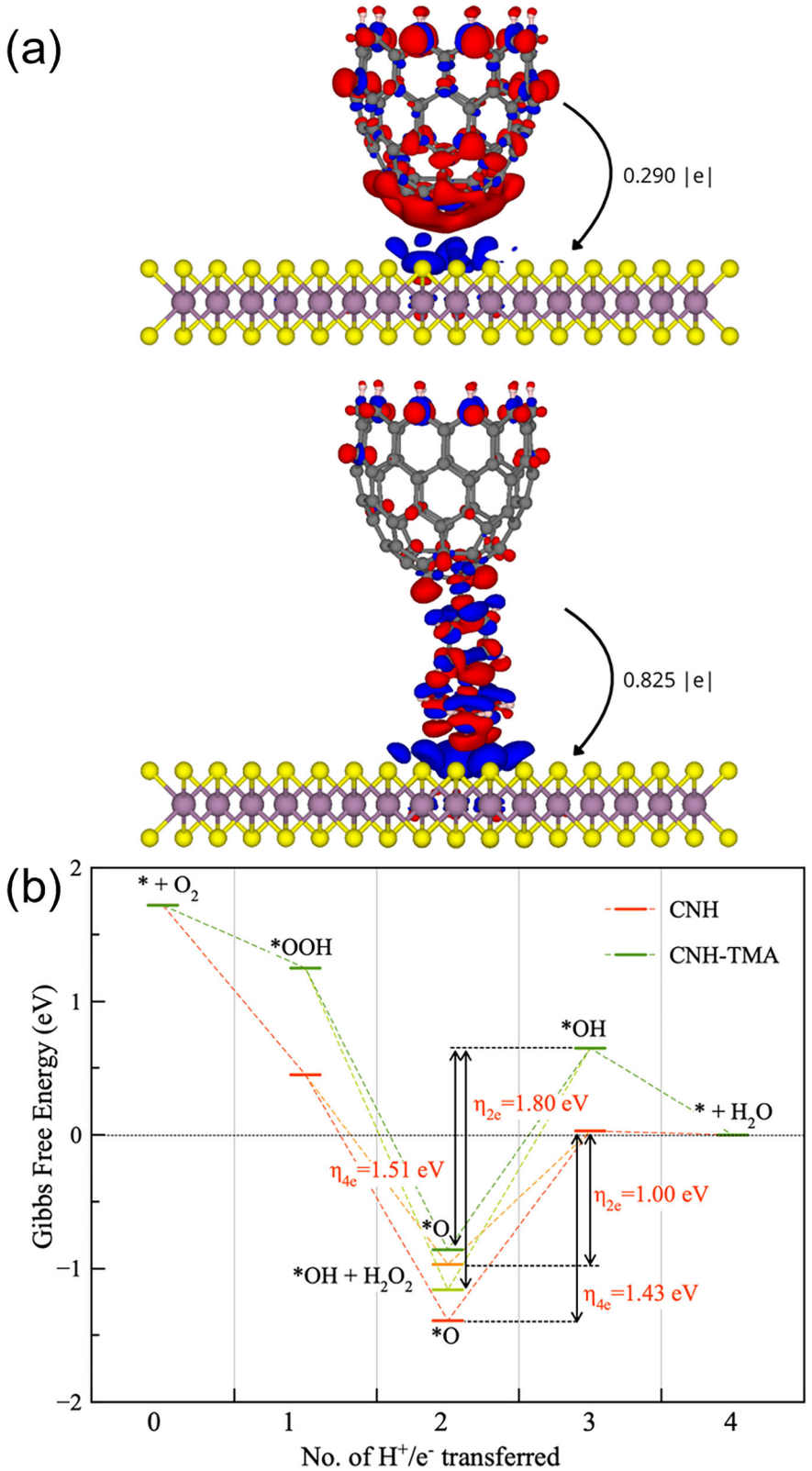



**Fig. 7 | Theoretical analysis of interfacial charge redistribution and ORR energetics on CNH-$MoS_2$ and CNH-N-$MoS_2$.** **a** Charge density difference plots for CNH-$MoS_2$ (top) and CNH-N-$MoS_2$ (bottom). The isosurfaces illustrate the interfacial charge redistribution upon formation of the heterostructures. Blue regions indicate electron density accumulation, whereas red regions indicate hole density accumulation. The values shown in the figure represent the amount of charge transfer, expressed in units of the elementary charge, (|e|). **b** Gibbs free energy diagrams for ORR on CNH-$MoS_2$ and CNH-N-$MoS_2$ at an applied bias of 0.8 V and pH 13. The red and green profiles correspond to CNH-$MoS_2$ and CNH-N-$MoS_2$, respectively. The ORR intermediates, including adsorbed OOH, O, and OH species, are indicated along the reaction coordinate as a function of the number of transferred proton/electron pairs. Light orange and light green symbols represent the $2e^-$ pathway, whereas red and green symbols represent the $4e^-$ pathway. The calculated overpotentials η are marked in red in the figure.

substantially larger for the modified system, going from a gain of 0.290 |e| in the CNH+$MoS_2$ model to up to 0.825 |e| for the CNH-N-$MoS_2$ interface, indicating a threefold increased propensity of electron transfer for the TMA modified heterojunction[47]. This trend is confirmed by the charge density difference shown in Fig. 6a, which provides a real-space visualization of electron depletion on the CNH side and electron accumulation on the $MoS_2$ side of the interface, which is strongly enhanced by the presence of the TMA.

These findings are also supported by the work function analysis. Although the total work function shift (Δϕ) remains nearly unchanged when comparing the two interfaces, varying from −1.40 eV for CNH +$MoS_2$ to −1.43 eV for CNH-N-$MoS_2$ its origin changes markedly. We

consider the work function shift as the sum of two contributions:

$$\Delta\phi = CT + \Delta V_{SAM}$$

where CT represents the charge transfer upon interface formation and $\Delta V_{SAM}$ the dipolar contribution of the CNH(-N) moiety. CNH+$MoS_2$ shows a negative $\Delta V_{SAM}$ contribution of −0.87 eV, leading to a relatively small negative charge transfer term of value − 0.53 eV. The functionalization of CNH with TMA leads to a reversal in the direction of its dipole moment, which becomes positive and has a value of 2.12 eV, resulting in a CT term being much more significant and negative −3.55 eV. Thus, the electronic properties analysis shows that the TMA modification of the interface favors the electron transfer process towards $MoS_2$. The negative shift in work function further confirms that the electron injection barrier is decreased, and the large amount of CT on the TMA-modified interface confirms its preference for the 4e- pathway for ORR over the $2e^-$ one.

To confirm these results, we performed further calculations on the catalytic activity of both interfaces and compared the propensity for both $2e^-$ and $4e^-$ pathways. The ORR intermediates — *OOH, *O, and *OH — were sequentially adsorbed on the selected S site of metallic 1T-$MoS_2$ at the interface. This approach is consistent with previous theoretical studies of $MoS_2$-based ORR systems, in which local electronic perturbations in sulfur-containing environments were shown to influence the oxygen reduction pathway[48,49].

Figure 7b reports the Gibbs free energy diagram for the ORR on both heterojunctions, when an applied bias of 0.8 V is applied (results in the absence of the bias are reported in Fig. S7). The 4e reaction path follows the classic intermediate formation, from $O_2$ adsorption to *OOH (where * indicates the catalytic substrate), *O, and *OH, while for the $2e^-$ reaction we consider the *OOH + $H_2O$ -> *OH + $H_2O_2$ intermediate, from which the release of $H_2O_2$ will lead to the *OH intermediate, which is the same as for the $4e^-$ pathway.

A first difference between the two models is their activity at zero bias, since CNH-N-$MoS_2$ follows almost perfectly the ideal catalyst (Fig. S8) for *OOH and *OH. However, both catalysts tend to strongly bind the *O intermediate, and the difference in this adsorption energy is the potential determining step (PDS) of the reaction and the key intermediate for the preference of the $4e^-$ over the $2e^-$ pathway for CNH-N-$MoS_2$. This strong absorption is reflected in the very short S-O bond, of 0.15 nm, compared to the longer *OOH and *OH bonds, with values in the 0.67-0.72 nm range (Table S2-4). According to Sabatier's principle, a too-strong adsorption energy is detrimental for catalysis, since the adsorbate can poison the catalyst and the reaction becomes sluggish. For the interface between pure CNH and $MoS_2$, the overpotential of the $4e^-$ pathway rises to 1.43 eV, while for the concomitant $2e^-$ path only 1.00 eV is required. Thus, the release of $H_2O_2$ towards the *OH intermediate is favored compared to the 4e-pathway through the *O intermediate, rationalizing the experimental finding of both $H_2O_2$ and water production on this catalyst.

The opposite scenario appears for the CNH-N-$MoS_2$ catalyst. Now, the formation of the 2e- key intermediate, *OH + $H_2O_2$ requires an overpotential of 1.80 eV, while the classic $4e^-$ pathway through the formation of the *O intermediate requires a lower overpotential of 1.51 eV. Thus, the classic $4e^-$ pathway is the favored one for the TMA-modified interface, rationalizing the selective water formation observed experimentally. This is further confirmed by the CT analysis on this PDS step, where a stronger electron depletion of −0.91 |e| is present on CNH-N-$MoS_2$ (compared to the -0.43 |e| on CNH-$MoS_2$), leading to a larger electron accumulation on the *O intermediate of 1.18 |e| (compared to the 1.10 |e| on CNH-$MoS_2$), confirming the improved electron transfer kinetics on the functionalized interface.

Collectively, these results demonstrate that the enhanced ORR activity and selectivity of CNH-N–$MoS_2$ arise from interfacial electronic modulation rather than from $MoS_2$ alone. While $MoS_2$ provides the catalytic active sites, the CNH-N support functions as an electron reservoir that facilitates charge delivery to the catalytic centers. Nitrogen functionalization further strengthens the interfacial electronic coupling by reducing the electron injection barrier, while the short interfacial separation (~4 Å) enables efficient charge transfer. Consequently, the functionalized heterointerface stabilizes the key *O intermediate, favors the four-electron reduction pathway over the competing two-electron route, and suppresses $H_2O_2$ formation, thereby rationalizing the experimentally observed high activity and selectivity toward $H_2O$ production.

## Discussion

This work presents a successful strategy for constructing highly efficient CNH-N–$MoS_2$ heterostructures through a stepwise covalent functionalization approach. Covalent grafting of TMA groups onto carbon CNHs enables the subsequent assembly of negatively charged 1T-$MoS_2$ nanosheets through strong electrostatic and interfacial interactions. Comprehensive spectroscopic, thermal, and microscopic characterizations confirm the successful functionalization of CNHs and the formation of the heterostructure. As a result, the CNH-N–$MoS_2$ catalyst exhibits significantly enhanced ORR performance, following a predominant four-electron pathway with approximately 94% selectivity toward $H_2O$, approaching the performance of commercial Pt/C catalysts under identical experimental conditions. The improved electrocatalytic activity is attributed to the synergistic effects of efficient interfacial charge transfer, the intrinsically high conductivity of 1T-$MoS_2$, and the intimate electronic coupling between $MoS_2$ and the nitrogen-functionalized CNH framework. Nevertheless, post-electrochemical characterization revealed partial oxidation of $MoS_2$, degradation of the heterostructure, increased disorder and oxygenation of the carbon framework, and probable catalyst loss, indicating that the long-term stability of the catalyst remains a challenge. Future efforts should therefore focus on improving the structural robustness and electrochemical durability of the heterostructure while preserving its excellent catalytic activity. Overall, this work demonstrates that covalently engineered carbon/TMDC heterostructures represent a promising class of low-cost, platinum-group-metal-free electrocatalysts for next-generation fuel-cell cathodes.

## Methods

### Materials preparation

CNHs were purchased from Carbonium S.r.l. (batch number LA102048A-0). All the other reagents and solvents were purchased from Sigma-Aldrich and used without further purification.

**1T-$MoS_2$ production**. 1T-$MoS_2$ was produced by a slightly modified lithiation procedure reported in the literature. A three-neck round-bottom flask was connected to an Ar Schlenk line and cleaned following standard Schlenk line procedure (cycles of vacuum, heating, and Ar flux), after which 1 g of bulk $MoS_2$ and a magnetic stirrer were added under Ar flux in the round-bottom flask and left drying under vacuum for 1 h at 40 °C. After drying, the glassware was cooled down using an ice bath, and then 4 mL of dry hexane was added, using an Ar-purged syringe, to the glassware under moderate stirring. Subsequently, 6 mL of LinBut in hexane was added in a similar way to the round-bottom flask. The ice bath was then removed, and the solution was left stirring for 3 days at room temperature. At the end of the reaction, the hexane solution was recovered using hexane as a solvent and centrifuged at 6000 rpm for 20 min, removing the supernatant and adding fresh hexane each time. This procedure was performed three times, and the final tubes were left drying under vacuum at 40 °C overnight. Subsequently, 800 mg of the as-lithiumed $MoS_2$ was added to 400 mL of deionized water and exfoliated using a tip-sonicator (TS, Bandelin Sonoplus), operating at 80% power output with 1 s on/1 s off cycles for 2 h while kept at 0 °C with an ice bath. The suspension was then centrifuged at 6000 rpm for 20 min and the supernatant was kept for further work. Furthermore, a set amount was freeze-dried to obtain 1T-$MoS_2$ powder for further characterization and to calculate the concentration of the suspension, which was 1 mg/mL on average.

**Synthesis of TMA-functionalized CNHs (CNH-N).** 30.0 mg (2.50 mmol) of CNH and 0.6947 g (2.50 mmol) of TMA iodide (synthesized according to a procedure reported in the literature) were dispersed into 17 mL of Milli-Q water[31]. The mixture was heated to 80 °C under N2 flow and magnetic stirring. Then 353 µL of isopentyl nitrite (2.50 mmol) was added. After 4 hours the reaction mixture was cooled to room temperature. The dispersion was filtered on a polycarbonate Isopore filter with 0.1 µm porosity. The product was washed with five 25 mL aliquots of a mixture of methanol and Milli-Q water (2:3) and five 25 mL aliquots of methanol. The functionalized product was removed from the filter by sonication in methanol and was dried under nitrogen flow.

**Synthesis of the hybrid materials.** For CNH-N-$MoS_2$, 10 mg of CNH-N was dispersed in 10 mL of Milli-Q water through bath sonication for 1 minute. The CNH-N dispersion was mixed with 1 mL of 1T-MoS2 dispersion in water with a concentration of 1 mg/mL. The mixture was decanted for 20 h and subsequently centrifuged at 5000 rpm for 5 minutes. The supernatant was removed, and the solid product was dried under a nitrogen flow. For CNH+$MoS_2$, 10 mg of CNHs and 1 mL of $MoS_2$ were mixed by sonication, then centrifuged at 5000 rpm for 5 minutes. The weight ratio of $MoS_2$ in both hybrid materials is 10%.

**Structural, chemical, and morphological characterization.** DLS measurements were carried out on a Zetasizer Nano S analyzer (Malvern Instruments, Malvern, UK). The measurement angle was set at 173°, backscatter (NIBS default). The analyses were carried out in a low-volume disposable plastic cuvette with a 1 cm optical path, in water at 25 °C, after an equilibration time of 120 seconds. The resulting value is an average of 3 measurements of 11 runs each, with a run duration of 10 seconds. Zeta Potential measurements were carried out in a clear disposable zeta cell, in NaCl 30 mM at 25 °C, waiting an equilibration time of 120 seconds. The theoretical model set for the measurement was the Smoluchowski equation. The resulting value is an average of 3 measurements of 10-100 runs each. To prepare the sample for DLS and Z potential, 5 mg of CNH-N was dispersed in 2.5 mL of Milli-Q water by pulsed microtip sonication for 1 minute and subsequent centrifugation at 10000 rpm for 10 min. The supernatant was recovered and filtered over cotton wool. The obtained dispersion, whose concentration was defined as the water dispersibility of CNH-N, was used to perform DLS and Z potential measurements. TGA measurements were carried out on a TGA Q5000IR of TA Instruments (TA Instruments, New Castle, DE, USA). The analyses were performed on a 100 µL Platinum-HT TGA pan in an $N_2$ atmosphere. The measurement method consists of an isotherm at 100 °C for 10 minutes followed by a 10 °C/min ramp to 1000 °C. TRIOS software has been used to process the thermograms. The concentration of CNH-N in water was evaluated by drop casting 1 mL of the CNH-N dispersion onto a calibrated TGA pan and then running an isotherm in air at 100 °C until constant weight. Raman spectra have been acquired with an Invia Renishaw Raman microspectrometer (20x objective). The solid samples were deposited on glass micro slides. The measurements were performed by irradiating the sample with a 633 nm He-Ne laser at room temperature for a time of 10 s. We characterized samples using a WITec confocal Raman system (α300-Raman WITec GmbH, Ulm, Germany), equipped with a 100X Zeiss objective, NA = 0.9, and a dispersive grating of 600 gr/mm that images a 100 µm core fiber, used to couple the microscope to the f = 320 mm spectrometer, as the input slit aperture on a 1 × 2048 pixels CCD (Newtown CCD, Andor, -80°C thermoelectric cooled). A solid-state laser, 532 nm, with a power of 14 mW, was used as the excitation line. The samples were dropped onto an n-type Si wafer. For the Raman spectra, each measurement was obtained by accumulating 80 spectra, each with an integration time of 25 s. Raman spectroscopy maps of 4 × 4 µm and 48 × 48 points were acquired at 2 seconds integration time per point. XPS spectra were acquired using a spectrometer manufactured by Physical Electronics GmbH (PHI 5000 VersaProbe II). TEM and HRTEM imaging were performed on a TALOS F200X (Thermo Fisher Scientific, Eindhoven, Netherlands) instrument without aberration correction, operating at an acceleration voltage of 200 kV. Images were captured using a 16-megapixel CMOS camera, and the FFT pattern was processed with Velox software (Thermo Scientific Velox Software, Thermo Fisher Scientific Inc., Waltham, MA, USA). Samples were prepared by dropping dilute suspensions of nanomaterials in ethanol onto carbon film-coated 200 mesh copper grids.

**Electrochemical characterization.** Electrochemical measurements were conducted in a three-electrode cell using a mercury-mercury oxide as reference electrode and a graphite rod as counter electrode. An RRDE tip with a glassy carbon (GC) disk (5 mm diameter) and a platinum ring was used as the working electrode. A thin-film catalyst layer was deposited by drop-casting on the GC electrode. The catalyst ink was prepared by mixing 2 mg of catalyst, 20 µL Nafion® (5 wt.%, Sigma-Aldrich), 50 µL ethanol, and 450 µL Milli-Q water. The ink was sonicated for 20 min to facilitate the dispersion of the catalyst, and then an aliquot of 10 µL was deposited on the GC. Linear sweep voltammetry (LSV) measurements in Ar- and $O_2$-saturated 0.1 M KOH (Sigma-Aldrich) were carried out to determine the activity towards the ORR. Then, LSVs were recorded at different rotation rates at 10 mV $s^{-1}$ in $O_2$-saturated 0.1 M KOH, while holding the Pt ring at +0.4 V, to determine the number of electrons transferred (n) and the percentage of hydrogen peroxide anion ($HO_2^-$) formed. The fraction of current due to $HO_2^-$ that is recorded by the ring electrode (%$HO_2^-$) and the corresponding electron transfer number during ORR ($ne^-$) were calculated by using the following equations:

$$\%HO_{2^-} = 100\frac{\boldsymbol{2Ir}}{\boldsymbol{IdN+Ir}} \quad (1)$$

$$n = \frac{4IdN}{IdN + Ir} \quad (2)$$

where $I_r$ is the ring current, $I_d$ is the disk current, and N is the collection efficiency (0.249). Currents reported are normalized by the electrode geometrical area (0.196 $cm^2$). The durability of CNH-N–$MoS_2$ was evaluated by CA at 0.68 V vs. RHE under air-saturated conditions using a Ti foil substrate (geometric area: 0.35 $cm^2$), which was selected to facilitate post-electrochemical characterization.

**Computational studies.** To gain insight into the origin of the improved ORR selectivity of CNH-N–$MoS_2$, periodic DFT calculations were performed with VASP within the plane-wave PAW formalism[50]. The CNH was described as a curved cone-like fragment, which is appropriate for carbon nanohorns and better reflects their local topology and, as a result, electronic structure[51]. The modified system contained one phenyltrimethylammonium (TMA) group covalently attached to the tip of the CNH.

All calculations were performed in vacuum using a hexagonal supercell with in-plane lattice parameters of 19.14 Å and a cell height of 36 Å. To eliminate polarization effects between the MoS2 monolayer and the CNH, vacuum layers with thicknesses of 21 Å and 15 Å were introduced above the systems. The initial interface structure was relaxed using a cutoff of $10-5$ eV for the total energy and 0.01 eV/Å for the maximum force. Dispersion corrections implemented in VASP were included to account for van der Waals interactions[52]. For the Bader charge analysis, the core electron densities were additionally reconstructed and included in the calculations. To visualize the Bader charge distribution, the charge density difference was calculated according to the equation:

$$\Delta\rho(r) = \rho(r)\mathrm{CNH}/1\mathrm{T} - \mathrm{MoS2} - \rho(r)\mathrm{CNH} - \rho(r)\mathrm{MoS2} \quad (3)$$

To obtain the Gibbs free energies of the ORR elementary reaction steps at 298 K, the Computational Hydrogen Electrode (CHE) framework was employed. The CHE model is one of the most widely used theoretical frameworks in electrocatalysis modeling. The CHE approach enables the calculation of electrochemical reaction free energies using DFT without explicitly modeling solvated protons and electrons. In this method, the chemical potential of a proton–electron pair is referenced to one-half of the chemical potential of gaseous hydrogen under standard conditions, according to the equilibrium:

$$H^+ + e^- = 1/2\,H_2$$

This simplification enables the evaluation of reaction energetics as a function of electrode potential and pH according to the following equation:

$$G(T) = E_0 + E_{ZPE} - TS + eU - 2.3RT/F\ pH \quad (4)$$

where $E_0$ is the electronic energy obtained from DFT calculations, EZPE is the zero-point energy correction, TS is the entropy contribution, U is the applied electrode potential[53–55]. During the structural optimization of the reaction intermediates, only the adsorbate and atoms up to the second nearest neighbor of the sulfur active-site S atom were allowed to relax, while all remaining atoms were constrained to their equilibrium positions. Geometry optimizations in the gas phase were followed by a single-point calculation in which the water solvent was considered with the PCM model. To obtain the vibrational contributions required for the calculation of ΔG of the reaction steps, a series of phonon calculations was performed using the frozen phonon approach. Atomic displacements of 0.015 Å were applied to construct the force constant matrix and evaluate the vibrational properties of the systems. During the phonon calculations, only the adsorbate and active site region were allowed to vibrate, whereas all other atoms were kept fixed. This approximation reduced the computational cost while preserving the local structural and electronic environment relevant to the adsorption process and catalytic activity.

## Data availability

The datasets generated and/or analyzed during the current study are not publicly available due to confidentiality but are available from the corresponding author on reasonable request.

Received: 25 June 2026; Accepted: 15 October 2026;
Published online: 07 November 2026

## References

1. León, M. I., Romero-Castañón, T., Flores-Hernández, J. R. & Nava, J. L. Experimental determination of HOR and ORR kinetic parameters in an AEMFC by the distribution of relaxation times method. *J. Power Sources* **629**, 236000 (2025).
2. Baglio, V., Martínez-Arias, A., Helsel, N. & Choudhury, P. Non-platinum group metal oxygen reduction catalysts for a hydrogen fuel cell cathode: a mini-review. *Catalysts 2025* **15**, 588 (2025).
3. Lee, J.-W. et al. Atomic-scale vacancy engineering unlocks basal-plane catalytic activity in metallic WSe2 for reversible oxygen electrocatalysis. *Mater. Sci. Eng.: R: Rep.* **169**, 101190 (2026).
4. Meng, F. et al. Rapid synthesis of single-layer iron-doped 2H tungsten sulfide via magnetic induction heating for piezocatalytic reduction of oxygen to hydrogen peroxide. *Appl. Catal. B: Environ. Energy* **371**, 125224 (2025).
5. Pozzati, M. et al. Systematic Investigation on the Surfactant-Assisted Liquid-Phase Exfoliation of MoS2 and WS2 in Water for Sustainable 2D Material Inks. *Phys. Status Solidi (RRL) – Rapid Res. Lett.* 2400039 https://doi.org/10.1002/PSSR.202400039. (2024).
6. Rowley-Neale, S. J., Smith, G. C. & Banks, C. E. Mass-producible 2D-MoS2-impregnated screen-printed electrodes that demonstrate efficient electrocatalysis toward the oxygen reduction reaction. *ACS Appl. Mater. Interfaces* **9** 22539–22548 (2017).
7. Xu, H. et al. Two-dimensional MoS2: structural properties, synthesis methods, and regulation strategies toward oxygen reduction. *Micromachines* **12**, 240 (2021).
8. Ma, Y. et al. Enhanced activities in alkaline hydrogen and oxygen evolution reactions on MoS2 electrocatalysts by in-plane sulfur defects coupled with transition metal doping. *Small* **18**, 2203173 (2022).
9. Upadhyay, S. N., Kumar, V., Sharma, N. & Pakhira, S. Enhanced catalytic performance of vanadium-doped MoS2 as a multifunctional electrocatalyst toward ORR, OER, and HER Applications. *ACS Appl. Energy Mater.* **8**, 8937–8949 (2025).
10. Boll, F. et al. In situ growth of layered 1T-MoS 2 onto carbon nanofibers as a strategy towards advanced hybrid materials for electrochemical energy storage and catalysis. *Nanoscale* **17**, 10706–10717 (2025).
11. Upadhyay, S. N., Joshi, H., Sharma, N. & Pakhira, S. Two-dimensional materials as emerging electrocatalysts for the HER, ORR, and OER: design strategies, challenges, and prospects in sustainable energy conversion. *Phys. Chem. Chem. Phys.* https://doi.org/10.1039/D6CP00222F (2026).
12. Amiinu, I. S. et al. Multifunctional Mo–N/C@MoS2 Electrocatalysts for HER, OER, ORR, and Zn–Air Batteries. *Adv. Funct. Mater.* **27**, 1702300 (2017).
13. Chua, X. J. et al. Negative Electrocatalytic Effects of p-Doping Niobium and Tantalum on MoS2 and WS2 for the Hydrogen Evolution Reaction and Oxygen Reduction Reaction. *ACS Catal.* **6**, 5724–5734 (2016).
14. Shrivastav, M., Kumar, V., Rana, K. & Dhiman, R. Oxygen reduction reaction kinetics of 2H-MoS2 and mixed-phase 1T/2H-MoS2 as a metal-free cathodic catalyst for PEM fuel cells. *J. Appl. Electrochem. 2024* **54**, 1517–1529 (2024).
15. Sebastian, M. M., Velayudham, P., Schechter, A. & Kalarikkal, N. Spinel Nickel Ferrite Nanoparticles Supported on a 1T/2H Mixed-Phase MoS2 Heterostructured Composite as a Bifunctional Electrocatalyst for Oxygen Evolution and Oxygen Reduction Reactions. *Energy Fuels* **36**, 7782–7794 (2022).
16. Meng, H. et al. Hybridization of iron phthalocyanine and MoS2 for high-efficiency and durable oxygen reduction reaction. *J. Energy Chem.* **71**, 528–538 (2022).
17. Wang, T. et al. Synergistic catalytic effect of MoS2 nanoparticles supported on gold nanoparticle films for a highly efficient oxygen reduction reaction. *ChemCatChem* **6**, 1877–1881 (2014).
18. Jayabal, S. et al. Understanding the high-electrocatalytic performance of two-dimensional MoS2 nanosheets and their composite materials. *J. Mater. Chem. A Mater.* **5**, 24540–24563 (2017).
19. Saini, R., Naaz, F., Bashal, A. H., Pandit, A. H. & Farooq, U. Recent advances in nitrogen-doped graphene-based heterostructures and composites: mechanism and active sites for electrochemical ORR and HER. *Green. Chem.* **26**, 57–102 (2024).
20. Hao, L. et al. Nitrogen-doped MoS2/carbon as highly oxygen-permeable and stable catalysts for oxygen reduction reaction in microbial fuel cells. *J. Power Sources* **339**, 68–79 (2017).
21. Moghaddam, M. S., Bahari, A. & Litkohi, H. R. Using the synergistic effects of MoS2/rGO and bimetallic hybrids as a high-performance nanoelectrocatalyst for oxygen reduction reaction. *Int. J. Hydrog. Energy* **48**, 33139–33154 (2023).
22. Zhang, S. et al. A defect-rich ultrathin MoS 2 /rGO nanosheet electrocatalyst for the oxygen reduction reaction. *RSC Adv.* **11**, 24508–24514 (2021).
23. Vinoth, R. et al. Synergistically enhanced electrocatalytic performance of an N-Doped Graphene Quantum Dot-Decorated 3D

MoS2–graphene nanohybrid for oxygen reduction reaction. *ACS Omega* **1**, 971–980 (2016).
24. He, C. et al. Oxygen reduction reaction promoted by the strong coupling of MoS2 and SnS. *ACS Appl. Energy Mater.* **4**, 9498–9506 (2021).
25. Liu, X., Ying, Y. & Ping, J. Structure, synthesis, and sensing applications of single-walled carbon nanohorns. *Biosens. Bioelectron.* **167**, 112495 (2020).
26. Swain, M. et al. Synergistic enhancement in energy storage in lithium/sodium ion batteries using engineered composites of MXenes and carbon nanohorns. *Nanoscale* **17**, 26077–26094 (2025).
27. Zafar, A., Ji, Z., Marco-Guimbao, J. & Delgado, J. L. Functional carbon nanomaterials in perovskite-based solar cells: from fullerenes to carbon nanohorns. *ACS Appl. Electron. Mater.* **7**, 6721–6732 (2025).
28. Feng, T. et al. Functionalized multi-walled carbon nanotube enhanced myogenic differentiation for aligned topography-induced skeletal muscle engineering. *Small* **21**, 2504992 (2025).
29. Suarato, G. et al. Modified carbon nanotubes favor fibroblast growth by tuning the cell membrane potential. *ACS Appl. Mater. Interfaces* **16**, 3093–3105 (2024).
30. Ceroni, L. et al. Quaternary ammonium-functionalized carbon nanotubes/alginate nanocomposite hydrogels support myoblast growth and differentiation. *J. Mater. Chem. B* **13**, 8105–8120 (2025).
31. Hadad, C. et al. Positive graphene by chemical design: tuning supramolecular strategies for functional surfaces. *Chem. Commun.* **50**, 885–887 (2013).
32. Pagona, G., Karousis, N. & Tagmatarchis, N. Aryl diazonium functionalization of carbon nanohorns. *Carbon N. Y.* **46**, 604–610 (2008).
33. Peng, H. et al. High performance Fe- and N- Doped carbon catalyst with graphene structure for oxygen reduction. *Sci. Rep.* **3**, 1765 (2013).
34. Tosin, E., Gatti, T., Agnoli, S., Calvillo, L. & Menna, E. Nitrogen- and fluorine-doped carbon nanohorns as efficient metal-free oxygen reduction catalyst: role of the nitrogen groups. *Surfaces 2023* **6**, 227–238 (2023).
35. Pagona, G., Katerinopoulos, H. E. & Tagmatarchis, N. Synthesis, characterization, and photophysical properties of a carbon nanohorn–coumarin hybrid material. *Chem. Phys. Lett.* **516**, 76–81 (2011).
36. Crisci, M. et al. Easy Direct Functionalization of 2D MoS2 applied in covalent hybrids with PANI as dual blend supercapacitive materials. *Adv. Mater. Interfaces* 2400621 https://doi.org/10.1002/ADMI.202400621 (2024).
37. Domenici, S. et al. Hybrid Piezoresistive 2D MoS2/PEGDA/PANI Covalent Hydrogels for the Sensing of Low-to-Medium Pressure. *Small Struct*. **2400131**, (2024).
38. Gatti, T. et al. A D-π-A organic dye – Reduced graphene oxide covalent dyad as a new concept photosensitizer for light harvesting applications. *Carbon N. Y.* **115**, 746–753 (2017).
39. Jeon, Y. et al. Thermally stable imidazole/heteropoly acid composite as a heterogeneous catalyst for m-xylene ammoxidation. *Res. Chem. Intermed. 2021* **47**, 287–302 (2021).
40. Fan, H. et al. Synthesis of metal-phase-assisted 1T@2H-MoS2 nanosheet-coated black TiO2 spheres with visible light photocatalytic activities. *J. Mater. Sci. 2018* **53**, 10302–10312 (2018).
41. Gray, E. L. et al. Metallic 1T NaxMoS2 as Sulfur Host for Room Temperature Na–S Batteries. *ACS Nano* **20**, 15632–15640 (2026).
42. Lu, S., Shi, Y. & Zhang, B. Active Sites of Metal-Free Carbon Materials in Energy Electrocatalysis. *Adv. Mater.* e73313 https://doi.org/10.1002/ADMA.73313;PAGE:STRING:ARTICLE/CHAPTER (2026).
43. Karmodak, N. & Andreussi, O. Oxygen Evolution on MoS2 Edges: Activation through Surface Oxidation. *J. Phys. Chem. C.* **125**, 10397–10405 (2021).
44. Risplendi, F. et al. Single-atom cobalt on N-doped reduced graphene oxide pushes the oxygen reduction reaction toward 4-electron pathway. *npj 2D Mater. Appl. 2025* **9**, 83 (2025).
45. Wang, M. et al. Ruthenium-decorated cobalt selenide nanocrystals for hydrogen evolution. *ACS Appl. Nano Mater.* **2**, 5695–5703 (2019).
46. Bera, B., Kar, T., Chakraborty, A. & Neergat, M. Influence of nitrogen-doping in carbon on equivalent distributed resistance and capacitance – Implications to electrocatalysis of oxygen reduction reaction. *J. Electroanal. Chem.* **805**, 184–192 (2017).
47. Henkelman, G., Arnaldsson, A. & Jónsson, H. A fast and robust algorithm for Bader decomposition of charge density. *Comput. Mater. Sci.* **36**, 354–360 (2006).
48. Liu, C., Dong, H., Ji, Y., Hou, T. & Li, Y. Origin of the catalytic activity of phosphorus-doped MoS2 for oxygen reduction reaction (ORR) in alkaline solution: a theoretical study. *Sci. Rep.* **8**, 13292 (2018).
49. Lucchetti, L. E. B., de Almeida, J. M. & Siahrostami, S. Revolutionizing ORR catalyst design through computational methodologies and materials informatics. *EES Catal.* **2**, 1037–1058 (2024).
50. Kresse, G. & Joubert, D. From ultrasoft pseudopotentials to the projector augmented-wave method. *Phys. Rev. B* **59**, 1758 (1999).
51. Karousis, N., Suarez-Martinez, I., Ewels, C. P. & Tagmatarchis, N. Structure, properties, functionalization, and applications of carbon nanohorns. *Chem. Rev.* **116**, 4850–4883 (2016).
52. Grimme, S., Antony, J., Ehrlich, S. & Krieg, H. A consistent and accurate ab initio parametrization of density functional dispersion correction (DFT-D) for the 94 elements H-Pu. *J. Chem. Phys.* **132**, 154104 (2010).
53. Alfonso, D. R., Tafen, D. N. & Kauffmann, D. R. First-principles modeling in heterogeneous electrocatalysis. *Catalysts 2018* **8**, 424 (2018).
54. Rossmeisl, J. et al. Calculated phase diagrams for the electrochemical oxidation and reduction of water over Pt(111). *J. Phys. Chem. B* **110**, 21833–21839 (2006).
55. Nørskov, J. K. et al. Origin of the overpotential for oxygen reduction at a fuel-cell cathode. *J. Phys. Chem. B* **108**, 17886–17892 (2004).
56. González-Gaitán, C., Ruiz-Rosas, R., Morallón, E. & Cazorla-Amorós, D. Functionalization of carbon nanotubes using aminobenzene acids and electrochemical methods. Electroactivity for the oxygen reduction reaction. *Int. J. Hydrog. Energy* **40**, 11242–11253 (2015).
57. Sandhiya, S., Saravanan, R. & Elumalai, P. Defect-engineered exfoliated MoS2/rGO hybrids for dual-function oxygen electrocatalysis and high-capacity Li-O2 batteries. *J. Power Sources* **674**, 239800 (2026).
58. Li, Q. et al. Investigating the role of Fe-Pyrrolic N4 configuration in the oxygen reduction reaction via covalently bound porphyrin functionalized carbon nanotubes. *Adv. Funct. Mater.* **34**, 2311086 (2024).
59. Tuci, G. et al. Chemically functionalized carbon nanotubes with pyridine groups as easily tunable N-decorated nanomaterials for the oxygen reduction reaction in alkaline medium. *Chem. Mater.* **26**, 3460–3470 (2014).
60. Lee, C. et al. $MoS_2$–carbon nanotube porous 3D network for enhanced oxygen reduction reaction. *ChemSusChem* **11**, 2960–2966 (2018).
61. Li, Q. et al. Investigating the effect of Fe–N5 configuration in the oxygen reduction reaction using N-heterocycle functionalized carbon nanotubes. *J. Mater. Chem. A Mater.* **12**, 28074–28084 (2024).
62. Shrivastav, M. et al. Enhancement in ORR performance by compositing Ni-decorated MoS2 with rGO for alkaline fuel cells. *Electrocatalysis* **16**, 349–359 (2025).
63. Xu, Y. et al. Pyridine functionalized carbon nanotubes: unveiling the role of external pyridinic nitrogen sites for the oxygen reduction reaction. *Small* **19**, 2302795 (2023).

64. Zhang, S. et al. A defect-rich ultrathin MoS2/rGO nanosheet electrocatalyst for the oxygen reduction reaction. *RSC Adv.* **11**, 24508–24514 (2021).

## Acknowledgements

Not applicable.

## Author contributions

M.W. performed conceptualization, data curation, Raman mapping measurement and analysis, investigation, wrote the original draft, reviewed, and edited the final manuscript. S.B. performed the Raman spectra and analysis. L. Cieszyński and S.O. performed DFT calculations, reviewed and edited the manuscript. M.C. synthesized 1T MoS2 and performed XPS measurements. M.P., Y.W. and Y.Z. reviewed and edited the manuscript. L. Calvillo performed ORR measurements and the XPS analysis, and reviewed and edited the manuscript. E.M., J.Z. and T.G. provided resources, reviewed, and edited the final manuscript.

## Funding

This work was supported by the European Research Council through project JANUS BI (ID: 101041229). S.O. thanks the Polish National Science Centre for funding (grant number UMO-2023/50/E/ST4/00197). We gratefully acknowledge the Polish high-performance computing infrastructure PLGrid (HPC Center: ACK Cyfronet AGH) for providing computer facilities and support within the computational grant number PLG/2026/019113. E.M. thanks the University of Padova (P-DiSC#07BIRD2026-UNIPD) for funding. Y. Z. thanks the European Union under the REFRESH-Research Excellence For REgion Sustainability and High-tech Industries (project number CZ.10.03.01/00/22_003/0000048) via the Operational Programme Just Transition.

## Competing interests

Teresa Gatti is an Associate Editor of npj 2D Materials and Applications. Teresa Gatti was not involved in the journal's review of, or decisions related to, this manuscript. The authors declare no competing financial or non-financial interests.

## Additional information

**Supplementary information** The online version contains supplementary material available at https://doi.org/10.1038/s41699-026-00752-8.

**Correspondence** and requests for materials should be addressed to Mengjiao Wang, Enzo Menna or Teresa Gatti.

**Reprints and permissions information** is available at http://www.nature.com/reprints

**Publisher's note** Springer Nature remains neutral with regard to jurisdictional claims in published maps and institutional affiliations.

**Open Access** This article is licensed under a Creative Commons Attribution 4.0 International License, which permits use, sharing, adaptation, distribution and reproduction in any medium or format, as long as you give appropriate credit to the original author(s) and the source, provide a link to the Creative Commons licence, and indicate if changes were made. The images or other third party material in this article are included in the article's Creative Commons licence, unless indicated otherwise in a credit line to the material. If material is not included in the article's Creative Commons licence and your intended use is not permitted by statutory regulation or exceeds the permitted use, you will need to obtain permission directly from the copyright holder. To view a copy of this licence, visit http://creativecommons.org/licenses/by/4.0/.

© The Author(s) 2026

This Article in Press is shared early to give you faster access to new research. It is citable and carries a permanent DOI. The final edited version will replace it automatically.